Key Points:

- We present the first crustal 3D *P*- and *S*-wave velocity model covering the entire Greater Alpine region (GAR) using Local Earthquake tomography
- We image a consistent decrease in velocity at mid crustal depths beneath the Western and Central Alpine arc
- We illuminate the seismic signature of the Dolomites indenter with a sharp velocity contrast on its western boundary along the Giudicarie line

Author Contributions:
Conceptualization: Benedikt Braszus, Andreas Rietbrock, Christian Haberland
Data curation: Benedikt Braszus
Formal analysis: Benedikt Braszus
Funding acquisition: Andreas Rietbrock, Christian Haberland
Methodology: Benedikt Braszus, Andreas Rietbrock
Project administration: Andreas Rietbrock, Christian Haberland
Supervision: Andreas Rietbrock, Christian Haberland

A 3D Velocity Model for the European Alps: New Insights Into the Crustal Structure

Benedikt Braszus[1], Andreas Rietbrock[1] [ID], and Christian Haberland[2]

[1]Geophysical Institute (GPI), Karlsruhe Institute of Technology, Karlsruhe, Germany, [2]Deutsches GeoForschungsZentrum GFZ, Potsdam, Germany

Abstract We present the first crustal 3D *P*- and *S*-wave velocity model covering the entire Greater Alpine region (GAR) based on Local Earthquake tomography. Applying the deep neural network PhaseNet to broad-band waveforms from 989 stations in the GAR between 2016 and 2022, we determined 173,841 *P*- and 68,967 *S*-phase onsets from 2,553 events with $M_L \geq 1.5$ recorded at epicentral distances up to 1,000 km. With the SIMUL2023 algorithm we simultaneously relocate the seismicity and invert for 3D velocity structure using an approximate bayesian approach to minimize the influence of the starting model. The excellent overall agreement with previously published geophysical transects gives us the confidence that our new 3D model is representative for the whole Alpine region. We find a consistent decrease in *P*- and *S*-wave velocity at mid crustal depths beneath the Western, Central and Eastern arc which we name the Alpine Mid Crustal Low Velocity (AMCLV) anomaly. The AMCLV is terminated sharply by the Dolomites indenter east of the Giudicarie line and is visible again east of 12°E, but considerably less pronounced in the Eastern Alps. Due to its partial connection to the upper crust in the European foreland we interpret this material to be formerly part of the European upper crust which has been stacked during the collision process. Based on 1D velocity profiles we suggest that the southern part of the Dolomites indenter consists mainly of undeformed northward dipping Adriatic mantle, whereas the northern part shows a thickened lower crust maybe caused by Permian intrusions.

Plain Language Summary The geophysical technique of seismic tomography has been used for many decades to resolve the physical properties of Earth's interior reaching from the uppermost meters to depths of several thousands of kilometers. Generally, seismometers are used to observe seismic waves that carry information about the part of the subsurface through which they traveled. In this study we combine the latest high-quality seismometer data from the European Alps and surrounding regions together with the recent progress in AI based seismological data analysis to compute the first consistently processed high-resolution *P*- and *S*-wave velocity model. In the Western and Central Alps we find untypical low propagation velocities of seismic waves in mid crustal depth of 15–25 km. We attribute this anomaly to the presence of formerly upper crustal material now residing in the middle crust as a consequence of crustal shortening and stacking during the continental collision which formed the Alpine mountain chain.

1. Introduction

With the closing of the Alpine Tethys at 35 Ma, the Europe-Adria plate boundary was transformed into a NW–SE oriented continental collision zone along which the Alpine mountain chain began to form (Carminati et al., 2012; M. Handy et al., 2010). Subsequently, Miocene counterclockwise rotation of the Adriatic plate relative to Europe and Africa caused a change in convergence direction from NW–SE to WNW–ESE and a decrease in convergence velocity in the Central and Eastern Alps relative to the Western Alps (Dewey et al., 1989). As a result, increased crustal shortening in the Western and Western Central Alps has lead to a crustal root of ≈60 km thickness (Spada et al., 2012). Shallower Moho depths in the Eastern Alps are a consequence of eastwards extrusion of crustal material toward the Pannonian basin (Ratschbacher et al., 1991).

A simplified map of the present geological setting in the Greater Alpine region (GAR) including the main tectonic units and fault lines is shown in Figure 1. The northern and southern Alpine foreland regions are characterized by the sedimentary Molasse and Po basin, respectively. A well-known feature at the western end of the Po basin is the Ivrea body which is imaged clearly by seismic (Diehl et al., 2009; Solarino et al., 2018; Thouvenot et al., 1996) and gravity studies (Bayer et al., 1989). It consists of oversteepened Adriatic mantle material overlying the eastwards subducting European crust (Zhao et al., 2020). In the Southern Alps, the northern part of the Adriatic

Writing – original draft:
Benedikt Braszus
Writing – review & editing:
Andreas Rietbrock, Christian Haberland
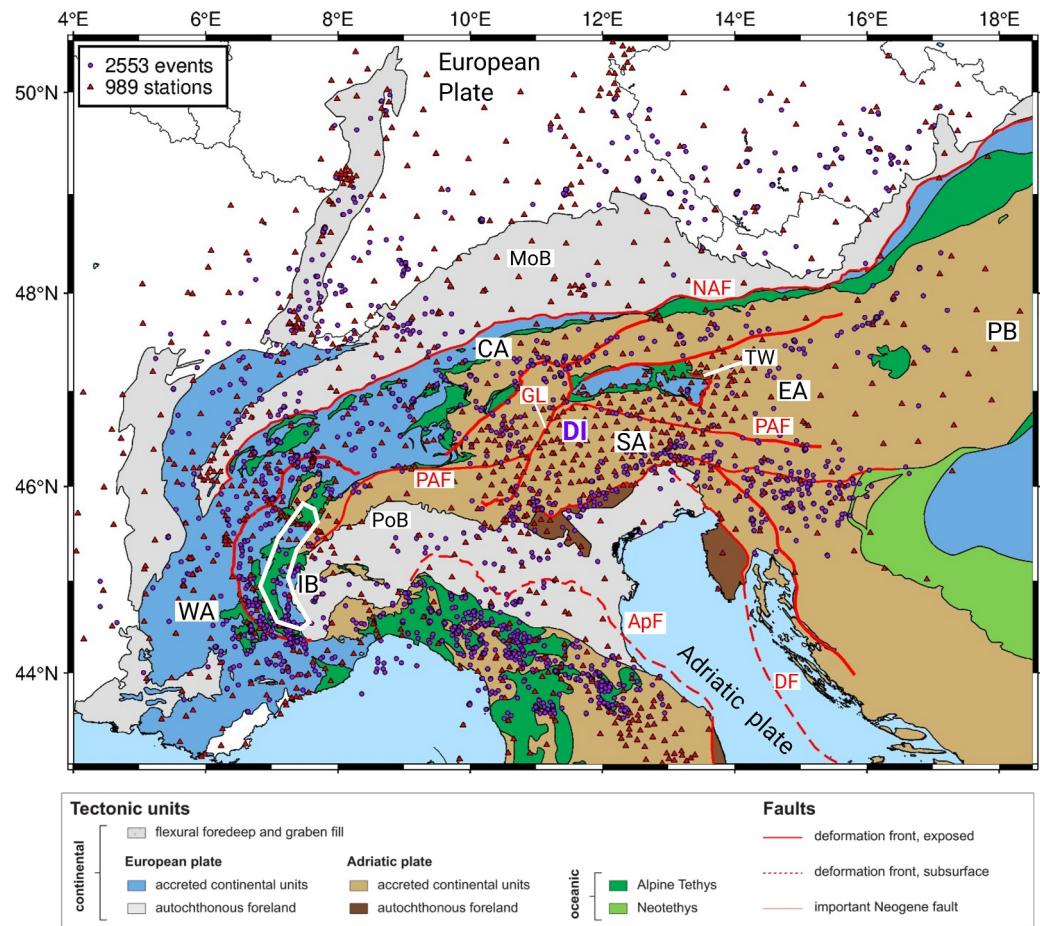
Figure 1. Slight modification of the tectonic map for the Greater Alpine region compiled by M.R. Handy with units and major lineaments simplified from Schmid et al. (2004, 2008); M. Handy et al. (2010, 2014); M. R. Handy et al. (2019); Bigi et al. (1990); Froitzheim et al. (1996); Bousquet et al. (2012). The dense station spacing of the AASN (Hetényi, Molinari, et al., 2018) is complemented by the SWATH-D (Heit et al., 2021) and CIFALPS2 (Zhao et al., 2018) networks leading to a total of 989 seismic broad-band stations with ≥5 observations. 2,553 events with $M_L \geq 1.5$ between 01/2016 and 12/2022 are predominantly based on Bagagli et al. (2022) and augmented by EPOS-EMSC (https://www.seismicportal.eu/), RESIF (https://franceseisme.fr/) and INGV (Arcoraci et al., 2020). NAF—Northern Alpine Front, PAF—Periadriatic Fault, GL—Giudicarie line, DF—Dinaric Front, ApF—Apenninic Front, TW—Tauern Window, PoB—Po Basin, MoB—Molasse Basin, PB—Pannonian Basin, WA—Western Alps, CA—Central Alps, SA—Southern Alps, EA—Eastern Alps, IB—Ivrea body.

plate indented into the European plate causing the W-E oriented Periadriatic fault to be offset sinistrally by the Giudicarie line (Pomella et al., 2012). This indenting body has been referred to as Southalpine indenter (e.g., Pomella et al., 2012), Adriatic indenter (e.g., Jozi Najafabadi et al., 2022; Kästle et al., 2024) and Dolomites indenter (e.g., Reiter et al., 2018). We consistently use the term *Dolomites intender* to describe this area delimited by the Giudicarie line and the Periadriatic fault to the West and North, respectively (Figure 1). Important information about the deeper (crustal and upper mantle) structure of the orogen at high resolution came from deep seismic sounding (reflection and refraction seismic experiments) mainly along orogen-perpendicular profiles. Among them are the ECORS-CROP profile (e.g., ECORS-CROP DSS Group, 1989), the NFP 20W profile (e.g., Levato et al., 1993), the EGT/NFP20E profile (e.g., Valasek et al., 1991), the TRANSALP profile (e.g., Lüschen et al., 2004), and the ALP2002 profile (e.g., Brückl, 2011; Hammerl & Brückl, 2014, and references therein). Since about 15 years, controlled source seismic activities along profiles were complemented by passive seismic recordings along the transects. Examples for these approaches are the TRANSALP (Gebrande et al., 2006), ALP2002 (Brückl et al., 2003), CIFALPS (Zhao et al., 2016), and EASI (Hetényi, Plomerová, et al., 2018) projects. Although these projects provided detailed images of the crust and lithosphere along 2D profiles at high resolution (e.g., Bleibinhaus and Gebrande, 2006; Brückl, 2011; Kummerow et al., 2004), the 3D-structure of the

GAR, obviously due to the strong variations of the Alpine arc, was hardly captured and is still not completely understood to date. This is especially true for the central Alpine region where it is not clear how the transition from the western to the eastern Alps, showing significant structural differences, is accommodated. Among the still discussed features along the Alpine chain are the slab dip (e.g., Lippitsch et al., 2003) or the presence and nature of a lower crustal wedge (Kissling et al., 2006), and—in turn—their geodynamic implications.

Within the scope of the recent interdisciplinary AlpArray/4DMB project a wide range of geoscientific studies have been conducted to further advance the understanding of the orogenesis of the European Alpine mountain chain. In this context the AlpArray Seismic Network (AASN) (Hetényi, Molinari, et al., 2018) and the complementary SWATH-D (Heit et al., 2021) and CIFALPS2 networks (Zhao et al., 2018) have been installed across the GAR providing an unprecedented uniform broad-band station spacing of ≈50 km (Figure 1). The most recent 3D P-wave model of the GAR by Bagagli et al. (2025) is based on seismic data from 1996 to 2019 including the AASN and used the *ADAPT* algorithm (Bagagli et al., 2022) to determine 84,326 P-phase onset times.

In this study we combine the AASN data set and its complementary networks, a recent 1D velocity model of the GAR (Braszus et al., 2024) and the rapid improvement of machine learning based seismic picking algorithms (Mousavi et al., 2020; Weiqiang & Beroza, 2018; Woollam et al., 2022). Thus we are able to compute the first uniformly processed orogen-wide 3D crustal P- and S-wave velocity model of the Alpine mountain chain and the northern Apennines based on 173,841 P- and 68,967 S-phase arrivals. We assess large scale differences in velocity structure along the Alpine arc, especially at mid and lower crustal depths and image the seismic signature of the Dolomites indenter in higher detail than previous studies (e.g., Diehl et al., 2009; Jozi Najafabadi et al., 2022; Kästle et al., 2018).

2. Data and Methods

This section gives an overview of the overall workflow including data processing, seismic phase picking and details on the inversion technique.

2.1. Waveform Data

We collected waveforms recorded by a total of 1,252 seismic broad-band stations within the GAR between 01/2016 and 12/2022. The majority of stations belongs to the AASN (Hetényi, Molinari, et al., 2018) which has been installed within the interdisciplinary European AlpArray research initiative. Additionally, we use data from the SWATH-D (Heit et al., 2021) and CIFALPS (Zhao et al., 2018) temporal deployments. All station XML data and raw waveform data is downloaded via the ObsPy FSDN Clients (Krischer et al., 2015) of the data hosting institutions. We are only considering three component stations with a sampling rate of ≥100 Hz and channels of either "HH?," "BH?" or "EH?." We resample all data to 100 Hz which is the required input sampling rate of the deep neural network *PhaseNet* (Weiqiang & Beroza, 2018) used for automatic phase arrival time determination.

2.2. Event Catalog

The comprehensive seismicity analysis of the GAR from Bagagli et al. (2022) provides uniformly processed initial hypocentral parameters for the time period from 2016 to 2019. For the years from 2020 to 2022 we obtained event detections and starting locations from the EPOS-EMSC (https://www.seismicportal.eu/), RESIF (https://franceseisme.fr/) and INGV (Arcoraci et al., 2020) accessed through the ObsPy FDSN Client and removed duplicates between the catalogs.

We consider events with $M_L \geq 1.5$ yielding an initial catalog consisting of 4,580 events between 2016 and 2022.

2.3. Seismic Phase Picking

In our previous work (Braszus et al., 2024) we inverted for the 1D velocity structure of the GAR and assessed the performance of some of the most commonly applied AI seismic picking algorithms using the *SeisBench* toolbox (Woollam et al., 2022). We compared a high precision manual P-phase pick catalog from the broader Swiss area from Diehl et al. (2009) to *PhaseNet* (Weiqiang & Beroza, 2018), *EQTransformer* (Mousavi et al., 2020) and *GPD* (Ross et al., 2018) each retrained on several benchmark data sets as included in *SeisBench*. Based on a combination of accuracy, recall rate of manual picks and additional phases we found *PhaseNet* in its original version to perform best and decide to use it for seismic arrival time determination.

Braszus et al. (2024) compared *PhaseNet P-* and *S*-phase onset times to a manual reference pick catalog including 10,295 *P*- and 3,770 *S*-picks from 30 events of this study. The deviations of *PhaseNet* and manual picks are summarized in Table S1 in Supporting Information S1 and shown in Figure S1 in Supporting Information S1. Averaging over observations from all distances leads to an estimated pick accuracy of $\sigma_{arr,P} = 0.23$ s and $\sigma_{arr,S} = 0.40$ s for *P*- and *S*-phases, respectively.

2.4. Pre-Inversion Pick Selection

In order to consistently remove outliers and secondary phase arrivals from our pick catalog, we modified the *2-fit-method* developed by Braszus et al. (2024) (Figure S2 in Supporting Information S1). This data-driven pre-inversion pick selection method plots the reduced travel time over hypocentral distance and fits weighted linear regression lines through the *Pg* and *Pn* arrivals between 0 and 100 km and 250–700 km, respectively. Onsets within 4σ of the extrapolated *Pg* fit at distances $\geq$150 km are not considered for the *Pn* fit. Arrivals within 2σ of the fits are selected while the remaining picks are discarded. In contrast to the previous version we do not categorically remove picks within the blue corridor, but select them if they are within 2σ of their corresponding fit. For further detail on the *2-fit-method* we refer to Section 3.4 in Braszus et al. (2024). The application of the *2-fit-method* to *S*-phases is shown in Figure S3 in Supporting Information S1. Here, *P*-phases close to the synthetic *Sn* onset are considered to be *S*-phases which have been mislabeled by *PhaseNet*. All plots generated by the *2-fit-method* are inspected manually. Events where regression lines could not be determined robustly due to insufficient picks or a large number of outliers are discarded entirely.

We consider events with $\geq$8 *Pg*- and $\geq$4 *Sg*-phases which yields a catalog of 2,373 earthquakes and leaves a small area of poor coverage in the Po plain in Northern Italy. For this region we loosen the criteria to $\geq$8 *Pg*-phases only and thus add 180 events ensuring a more uniform ray coverage of the model space. Eventually, we discard events with a $GAP \geq 180°$, stations with <5 observations and all *S*-phases without a corresponding *P*-onset. *Pn* phases with epicentral distances of up to 1,080 km are obtained for 837 events including 26,000 *Pn* arrivals observed at distances $\geq$400 km.

This results in a final catalog of 242,808 arrivals consisting of 88,600 *Pg*, 55,921 *Sg*, 85,241 *Pn* and 13,046 *Sn* phases, respectively. The final locations of the 2,553 events and 989 stations with $\geq$5 phase records are shown in Figure 1.

2.5. Tomographic Inversion

We are using *SIMUL2023* (Eberhart-Phillips et al., 2024) which is the most recent version of the well-established *SIMULPS* algorithm (Eberhart-Phillips, 1990; Thurber, 1983) to simultaneously invert for hypocentral parameters and the *vp* and *vp/vs* structure of the model space. SIMUL2023 linearizes the coupled hypocenter-velocity problem around a starting model and iteratively minimizes the travel time residuals using a damped least squares approach. In each iteration step ray-tracing is performed by an efficient pseudo-bending algorithm (Um & Thurber, 1987). The model is parametrized on nodes which are located on the intersections of a rectangular grid. The velocity at an arbitrary point within the model space is defined by a linear B-spline interpolation of neighboring node values yielding a spatially smooth distribution of model parameters. It should be noted that such parameterizationa will not provide sharp velocity contrasts and therefore iso-proxy velocities have to be used to define depths of sharp velocity contrasts like the Moho.

Large distance observations can potentially negatively impact the hypocentral accuracy when included for seismicity (re)location (Diehl et al., 2021). Therefore, in a first inversion step we relocate the seismicity and invert for the upper crustal velocity structure using *P*-phases with $\Delta \leq 130$ km and *S*-phases with $\Delta \leq 80$ km. The resulting velocity model and hypocentral parameters are used as input for the second inversion step which is including picks from all distances while keeping the hypocenters fixed and only updating the origin time. In both inversions we are fixing the velocity at the outermost nodes and applying a constant linking to neighboring nodes in areas of poor resolution as indicated by spread values (Figure S4 in Supporting Information S1) which results in 12,053 independent velocity model parameters. We calculated trade-off curves for damping λ of *vp* and *vp/vs* for both inversions (Figure S5 in Supporting Information S1) and select damping values of $\lambda_{p1} = 1{,}000$; $\lambda_{ps1} = 1{,}000$ and $\lambda_{p2} = 5{,}000$; $\lambda_{ps2} = 4{,}000$, respectively. In the following we will refer to the two inversion steps as one single inversion run.

Based on checkerboard reconstruction tests for several parametrizations, we choose a horizontal node spacing of 25 km. Regarding the vertical node spacing, we find models with either six or seven nodal planes between 0 and 70 km depth to be most suitable. Models with larger spacing show a significantly increased data misfit, while a finer spacing introduces vertical smearing and insufficient reconstruction of synthetic models. The final data variances of $\sigma_{d,P}^2 \approx 0.18$ s^2 and $\sigma_{d,S}^2 \approx 0.22$ s^2 are significantly larger than the estimated picking uncertainties $\sigma_{arr,P}^2 = 0.05$ s and $\sigma_{arr,S}^2 = 0.16$ s (see Section 2.3) which indicates that model updates are still based on a distinguishable signal and no overfitting is taking place.

We determine the optimal vertical node spacing by running 750 inversions with variable node depths. Initial v_p velocities are taken from Braszus et al. (2024) who used a Markov chain Monte Carlo (McMC) approach (Ryberg & Haberland, 2019) to compute the *GAR1D_McMC* (DOI:10.35097/1965) *P*- and *S*-wave 1D model for the Alpine region including statistical uncertainties. We use a constant initial v_p/v_s ratio of 1.71 representing the average value of the *GAR1D_McMC* and perturb the initial v_p of each individual model by $\pm 1\sigma$ of the *GAR1D_McMC* model. Similarly, initial event locations are shifted horizontally and vertically by $\sigma_{hor} = 2.0$ km and $\sigma_{ver} = 6.0$ km based on the hypocenter uncertainty estimates of Braszus et al. (2024). Additionally, in each single run the entire grid is shifted randomly in *x*- and *y*-direction by ± 12.5 km which is equal to half the horizontal node spacing.

The evolution of data misfit over 20 iterations for 750 runs each with six and seven layers is shown in Figure S6 in Supporting Information S1. The variance reduction is largest in the first 5–6 iterations and significantly slows down after $\approx$10 iterations with only marginal improvements. We therefore consider the set of 750 runs with seven layers after 13 iterations for the final step where we average the best 20 models. Thus, the final model is smoother and not dependent on a single parametrization. Figure S7a in Supporting Information S1 shows the vertical node distributions that are yielding the smallest data variance for seven layers between 0 and 70 km and 13 iterations. Based on a previous test with completely arbitrary node distribution, we limit the range of randomly generated parametrizations to models with three nodes between 5 and 35 km, one node between 35 and 45 km and one node between 45 and 57 km. Since the final model is based on an average of 20 parametrizations, we define a reference layering for synthetic tests with nodes at 0, 10, 18, 28, 40, 55, and 70 km resembling the average node depths of the best 20 models. Averaging over a lower or higher number of individual models does not significantly affect the final result as shown in Figure S8 in Supporting Information S1. This indicates the robustness of the inversion, since each single run has been computed with shifted initial hypocenters, a perturbed 1D starting model and varying horizontal and vertical model parametrization.

2.6. Hypocenter Relocation

SIMUL2023 linearizes the coupled hypocenter-velocity problem around an initial model and iteratively updates hypocenters and velocity structure. Thus, it is crucial to evaluate the influence of the initial parameters on the final inversion result. A common way to do this are hypocenter shift tests (Haslinger et al., 1999; Husen et al., 1999) where initial hypocenters are moved horizontally and vertically in order to quantify the robustness of the resulting event locations and velocity models. If slight changes of the initial parameters lead to a strong variation in the inversion output, this would indicate an instable result. Our inversion approach as described in the previous section enhances the conventional shift test by additionally varying the initial 1D model within its uncertainties and testing a wide range of grid parametrizations. Each single event in each run has initially been shifted with $\sigma_{hor} = 2.0$ km and $\sigma_{ver} = 6.0$ km. Locations between all 750 runs are deviating by less than $\sigma_{hor} = 0.5$ km and $\sigma_{ver} = 3.5$ km for almost all events which indicates the robustness of the resulting hypocenters (Figure S9 in Supporting Information S1). Similar to the velocity model, we define our final event locations as the average hypocentral parameters of the 20 inversion runs with the lowest data misfit. The comparison of the initial hypocenters based on a 1D model including station corrections and our final hypocenters located in the 3D model yields deviations of $\sigma_{lat} = 1.67$ km, $\sigma_{lon} = 1.38$ km and $\sigma_{dep} = 4.67$ km in latitude, longitude and depth, respectively. This is in agreement with Braszus et al. (2024) who quantified the horizontal and vertical hypocenter accuracy as $\sigma_{hor} \approx 2.0$ km and $\sigma_{ver} \approx 6.0$ km, respectively, when using a 1D velocity model including station corrections for the GAR.

3. Model Resolution

There are a number of parameters that are commonly used to quantify the resolution such as the derivative weighted sum, hit count, resolution diagonal elements, and spread function (Diehl et al., 2009; Eberhart-Phillips, 1990; Toomey & Foulger, 1989). Another way to determine the resolution within certain regions of the model space are reconstruction tests. Travel times are calculated through a synthetic model and are then inverted using the same starting model as for the real data inversion. In order to simulate the effect of picking uncertainty, a noise term with the amplitude of the estimated picking error can be added to the synthetic travel times. The shape of the synthetic model can range from an equally spaced checkerboard over random complex structures to anomalies of expected size and amplitude.

The following summarizes the analysis we carried out to assess to resolution of our final velocity model. All tests are run as a joint inversion of picks from all distances with 5 iterations using a slightly decreased damping of $\lambda_p = 3,000$; $\lambda_{ps} = 3,000$. We choose a reference layering of 0, 10, 18, 28, 40, 55, and 70 km representing the average node depths of the individual runs contributing to the final model.

3.1. Spread Function

The spread function value is calculated for each node and quantifies the distribution of values around the diagonal matrix elements along each row of the model resolution matrix (MRM) (Toomey & Foulger, 1989). Nodes with low spread values are therefore better constrained than nodes with higher spread. Figures S10 and S11 show depth slices of spread function values for *vp* and *vp/vs*, respectively. At shallow depths areas of low spread are clearly correlating with the regions of increased seismicity in the Southwestern Alps and Northern Apennines and the area of dense station spacing of the SWATH-D network (Figure 1). The Western Po plain is showing rather large spread values in the upper 20 km due to its sparse seismicity and unfavorable recording conditions. With increasing depth the resolution of the model space becomes homogeneous as the number of criss-crossing and horizontally propagating rays is increasing. As aspired, this yields a fairly uniform spread value distribution at depths of 25–70 km for *vp* as well as *vp/vs*.

3.2. Checkerboard Tests

Checkerboard tests are a widely used tool to assess the solution quality of seismic tomography images (Diehl et al., 2009; Fukao et al., 1992; van der Hilst et al., 1993). Additionally, we use them to derive the finest model parametrization which still yields a robust reconstruction of synthetic anomalies. In our case this is a horizontal node spacing of 25 km and a vertical spacing of 10–15 km. To account for the estimated picking error (Section 2.3 and Braszus et al. (2024)), we add normally distributed noise with $\sigma = 0.25$ s to the synthetic *P*- and *S*-phase travel times.

In our models every second layer is perturbed with alternating anomalies of ±10% in either *vp* or *vp/vs* with every other layer remaining unperturbed. The reconstructed models with *vp* and *vp/vs* perturbations in even and odd numbered layers, respectively, are shown in Figures S12–S15.

Figure 2 shows the recovered checkerboard models together with contour lines of a spread function value of 2.5. Based on a combination of checkerboard test and spread function value we define the part of the model space which is resolved well enough to be interpreted. The poorly resolved areas are blurred.

3.3. Characteristic Model

To assess to which extend an anomaly with a certain shape and amplitude can be resolved, more realistic synthetic models are used for reconstruction tests (Haslinger et al., 1999). We perform recovery tests with normally distributed noise of $\sigma = 0.25$ s and arbitrarily chosen anomalies in every second layer. Additionally, we insert a π-shaped low velocity anomaly beneath the Central Alps which is encircling a small rectangle of six nodes with increased velocity just E of the Giudicarie line. These structures are resembling main features of our final inversion. A comprehensive comparison of initial and reconstructed model is shown in Figures S16 and S17 while Figure 3 shows the depth slices at 28 and 55 km.
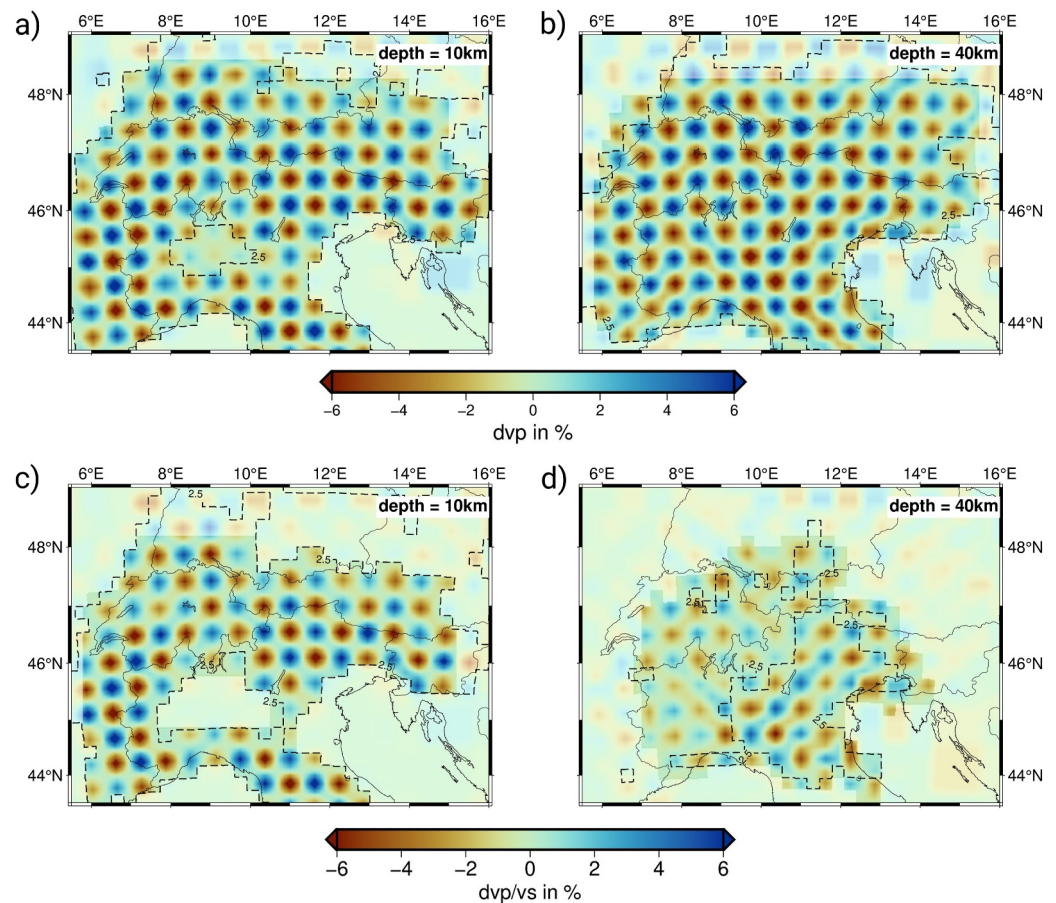
Figure 2. Recovery of *vp* (a and b) and *vp/vs* (c and d) checkerboard anomalies of ±10% and contour lines of spread values for selected depths. Based on a combination of checkerboard reconstruction and spread value we define the well resolved models parts and blur areas of poor resolution.

Anomalies of *vp* (Figures 3a and 3b) in the center of the model space are very well recovered in shape except for the most shallow layer at 0 km depth (Figure S17 in Supporting Information S1). In well resolved areas synthetic amplitudes of ±10% are recovered as 4–7%, which corresponds to about half their initial amplitude. The π-shaped low velocities and the high velocity rectangle are recovered accurately in shape with an amplitude of 4–6%.

Anomalies of ±10% in *vp/vs* are recovered as 2–3% at 28 km depth (Figure 3). At 55 km depth (Figure 3d) the reconstructed amplitude reaches 4–6% with moderate horizontal smearing.

4. Results

We summarize the most prominent features within the resolved models parts on the basis of depth slices and cross sections through our final velocity model.

4.1. Depth Slices

Figure 4 shows horizontal slices through the final *vp*, *vp/vs* and *vs* model at 6, 26, 34, and 44 km, respectively.

At shallow depths the Alpine orogen generally shows a slightly increased *vp* (Figure 4a) and a coherently decreased *vp/vs* ratio (Figure 4c) resulting in a substantial increase in *vs* (Figure 4e). A prominent low velocity zone is present for *vp* and *vs* in the Po basin in the southern foreland (anomaly A). Similarly, in the northern and western foreland a low *vp* and *vs* anomaly is extending along the Molasse basin (anomaly B). While the southern foreland shows a rather consistent increase in *vp/vs* (anomaly A), in the northern foreland an increased *vp/vs* is
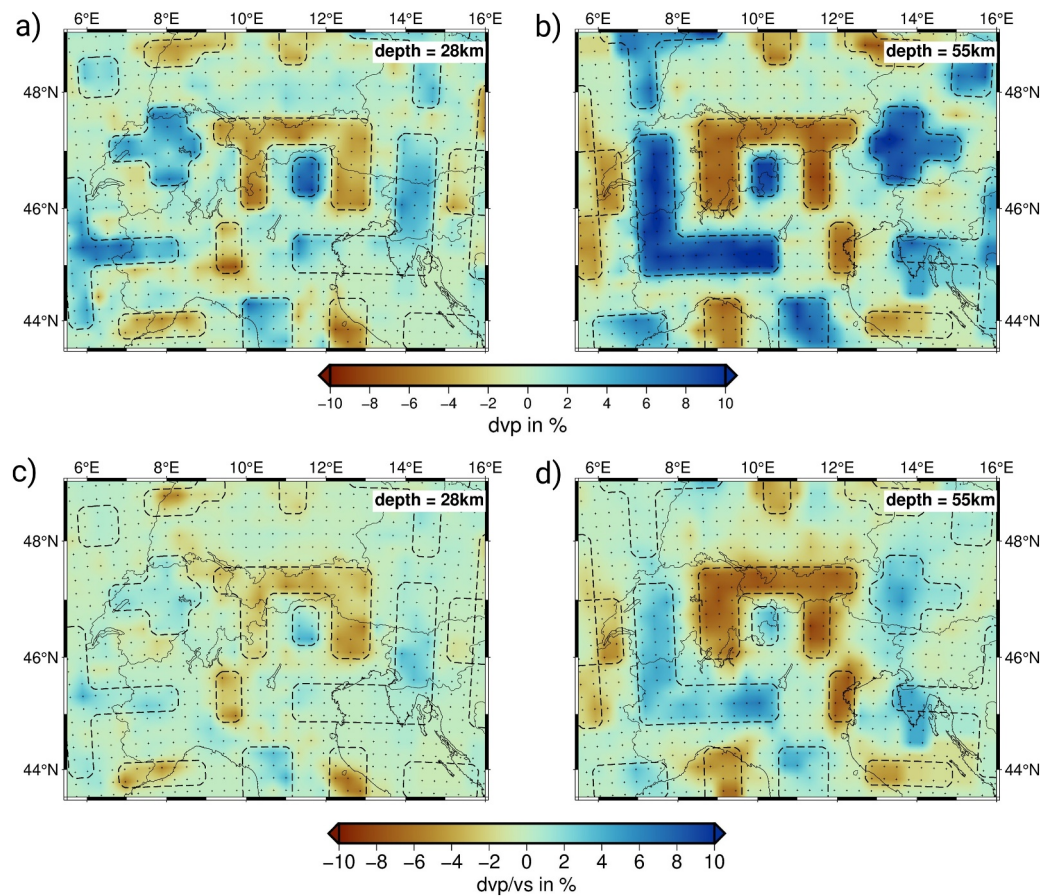
Figure 3. Reconstruction of characteristic models for v_p (a and b) and v_p/v_s (c and d) at 28 and 55 km depth. Outlines of the ±10% perturbations in the synthetic models are marked by dashed lines.

only present in the Eastern Molasse basin (anomaly B). Another area of strongly increased vp/vs is present in the Friaul region in northeastern Italy and western Slovenia (anomaly C).

Throughout the mid and lower crust a well-defined WNW-ESE trending zone of low velocities is present beneath the northern Apennine (anomaly D). Due to the increased vp/vs, the negative anomaly in v_s is more pronounced than in v_p. This feature is becoming thinner with depth and is visible up to 50–55 km. In the western Po plain a very strong and sharply delineated positive anomaly is visible in vp and vs in the region where previous studies found the Ivrea Geophysical body (anomaly E). This feature is strongest at 20–30 km (Figures 4b and 4f) where it is showing mantle velocities already without a noticeable vp/vs signature. South of the Central Alps a W-E elongated positive anomaly in vp and vs stretches from the Lago Maggiore to the Italian-Slovenian border along the northern Po plain (anomaly F).

At mid and lower crustal depths, the area beneath the Alpine arc is characterized by a decrease in vp and vs (anomalies G, H, K, L, M, N). Generally, there is a relatively thin band of low velocities following the Alpine arc west of ≈9.5°E (anomalies G, K, M). This low velocity area thickens toward the East until is reaches the Giudicarie Fault at ≈11°E (anomaly H, L, N). East of 12°E this anomaly is less distinct in shape and amplitude.

A region of increased vp and vs is present directly east of the Giudicarie Fault between 11 and 11.5°E at depth of 20–40 km (anomaly J). It is connected to the slightly elevated velocities beneath the Northern Po plain (anomaly F) and disrupts the otherwise continuous low velocities beneath the Alpine orogen.

Deeper than 20 km, there is no coherent feature in the v_p/v_s model, except for the increase beneath the northern Apennine (anomaly D).
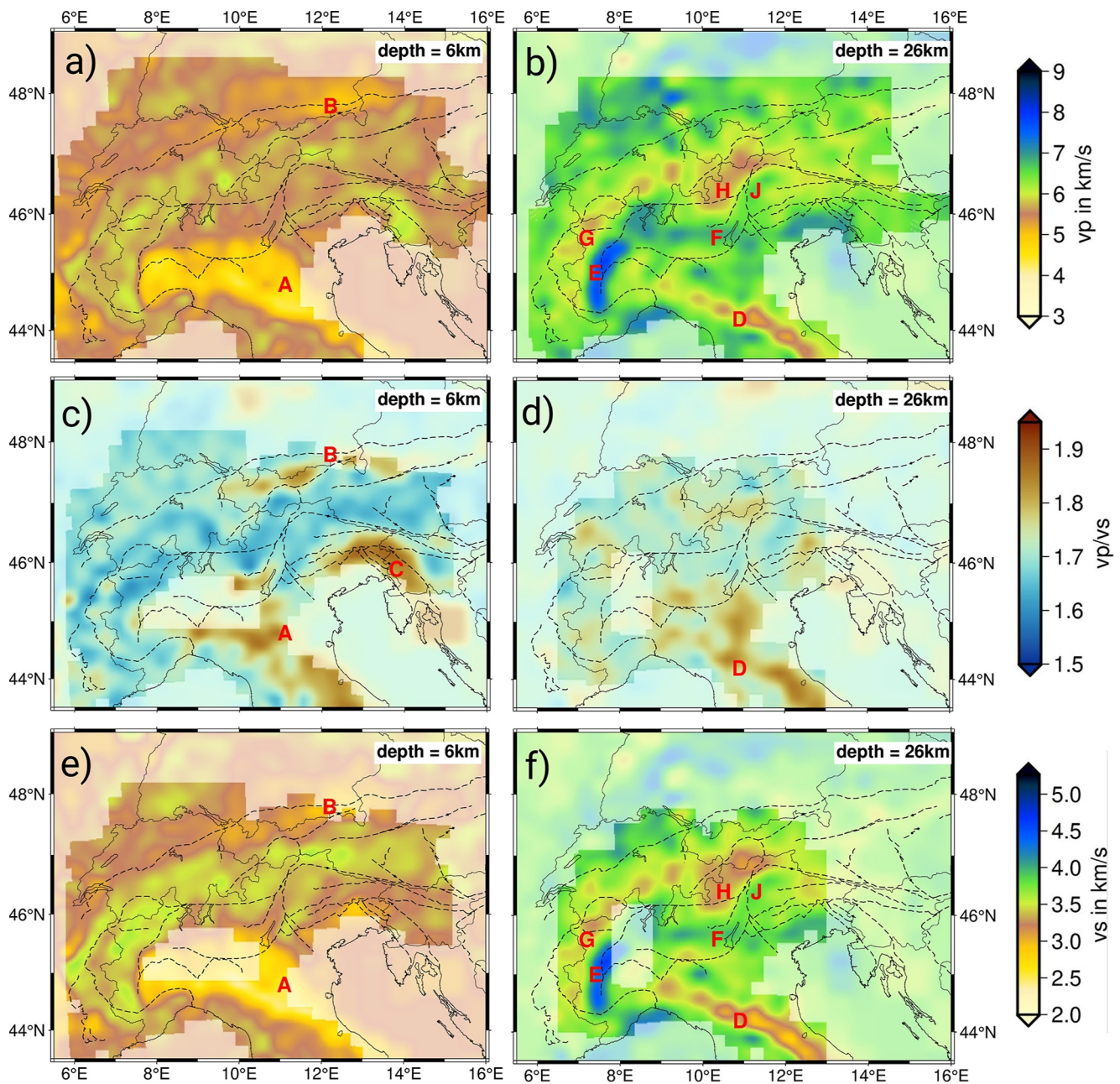
Figure 4. Horizontal slices through the final v_p, v_p/vs and v_s model for depths of 6 km (a, c, e), 26 km (b, d, f), 34 km (g, i, k), and 44 km (h, j, l), respectively. Areas of poor resolution (Figure 2) are blurred. For a description of anomalies A-N we refer to the text. Major fault lines (dashed) are based on Schmid et al. (2004). The colorbar for v_p and v_s is a modified version of Diehl et al. (2009).

4.2. Cross Sections

Figure 5 shows several cross sections of vp cutting perpendicular through the Alpine arc including the previously investigated CIFALPS, ECORS-CROP, TRANSALP and EASI transects. Similar to previous studies of the region (Diehl et al., 2009; Jozi Najafabadi et al., 2022) we plot the contour line of $vp = 7.25$ km/s (black dashed) as a Moho proxy. The Moho depth from Spada et al. (2012) is indicated by dashed white lines while the seismicity within 30 km of the corresponding profile is denoted by purple dots.

All profiles display shallow low velocity zones in the western or northern (anomaly B) as well as in the southern forelands (anomaly A) corresponding to the Molasse basin and Po basin, respectively. Beneath the eastern edge
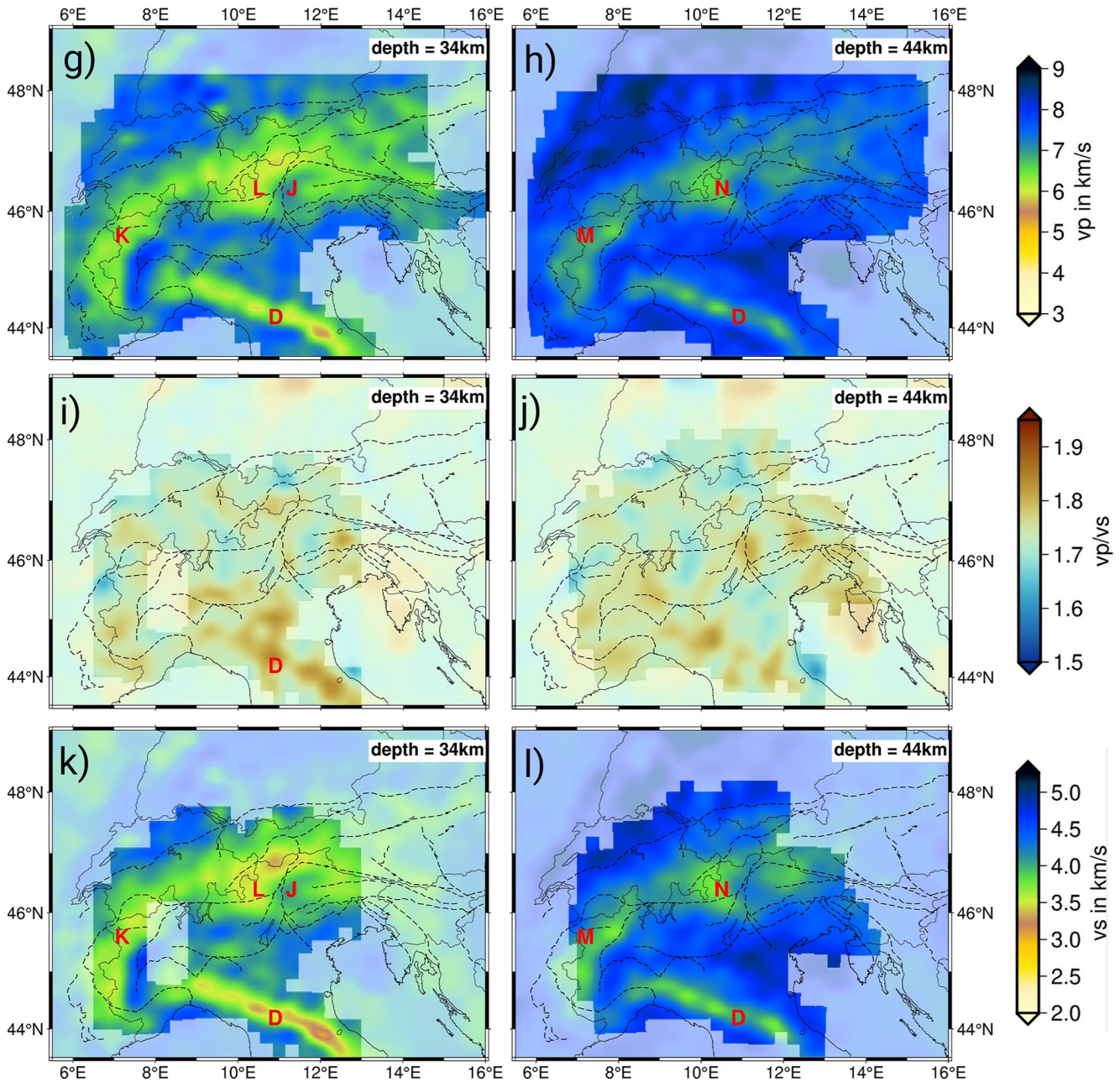
Figure 4. (Continued)

of the western Alpine arc, profiles 1 and 2 reveal a positive anomaly with mantle velocities present at mid-crustal depths coinciding well with the location of the Ivrea Body (anomaly E). On the western edge of the Ivrea body our Moho proxy jumps from 50 to 60 km depth on the European side to ≈20 km on the Adriatic side in Profiles 1 and 2. From there it shallows toward the W/NW beneath the European foreland while it deepens again underneath the northwestern Po basin on the Adriatic side. All profiles display an area of decreased vp at depths of 15–25 km beneath the mountain chain with varying shape and amplitude (anomalies G, H, and P). In profile 2 this feature is isolated from the very shallow low velocities while in profiles 1, 3, and 4 a connection to the surface is visible. Profile 5 is showing a slightly northward dipping positive anomaly (anomaly Q) in the upper
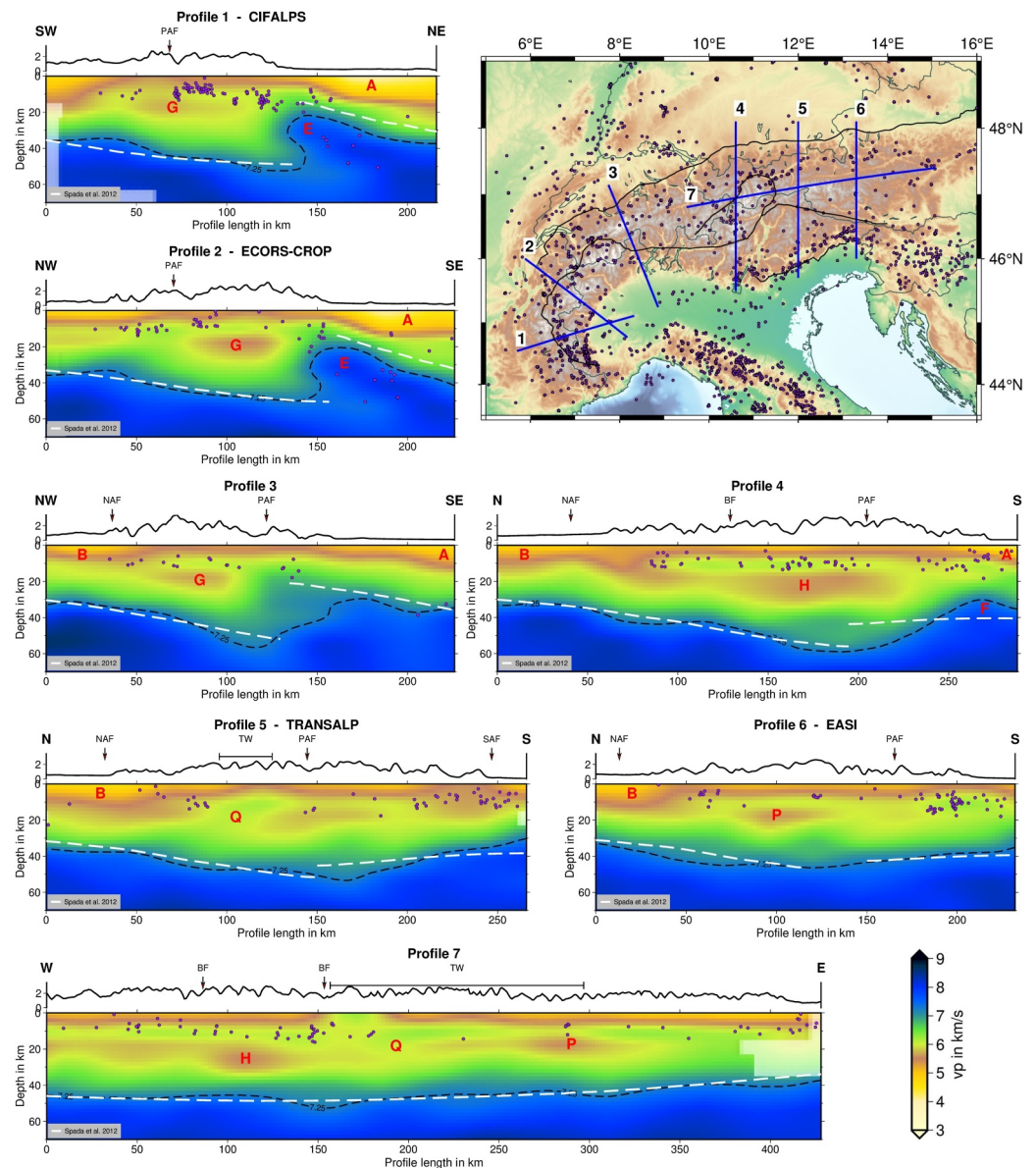
Figure 5. Cross sections through the final v_p model for several arc perpendicular profiles along the entire orogen and a W-E striking profile through the Central and Eastern Alps. Purple dots mark the seismicity within 30 km of the profile. Moho depths from Spada et al. (2012) and our Moho proxy of the $v_p = 7.25$ km/s isoline are shown as white and black dashed lines, respectively. Labels along the profile mark the intersection with major fault lines (Schmid et al., 2004): PAF—Periadriatic fault; NAF—Northern Alpine Front; BF—Brenner Fault; SAF—Southern Alpine Front; TW—Tauern Window.

20 km beneath the Tauern window next to a similarly northward dipping low velocity anomaly South of it. Along profile 4 in the Central Alps the Moho proxy reaches ≈60 km and dips considerably steeper on the Adriatic side (anomaly F) than on the European side. This difference in dip angle is evening out toward the East in profiles 5 and 6 while the maximum Moho depth decreases to ≈45 km in profile 6. The continuous shallowing of the Moho toward the East is also visible in profile 7. Here, the previously identified low velocities at 15–25 km depth (anomalies H and P) are present consistently except beneath the western Tauern window (anomaly Q). They are less pronounced and slightly shallower beneath the eastern Tauern window (anomaly P) and disappear East of 14°E.
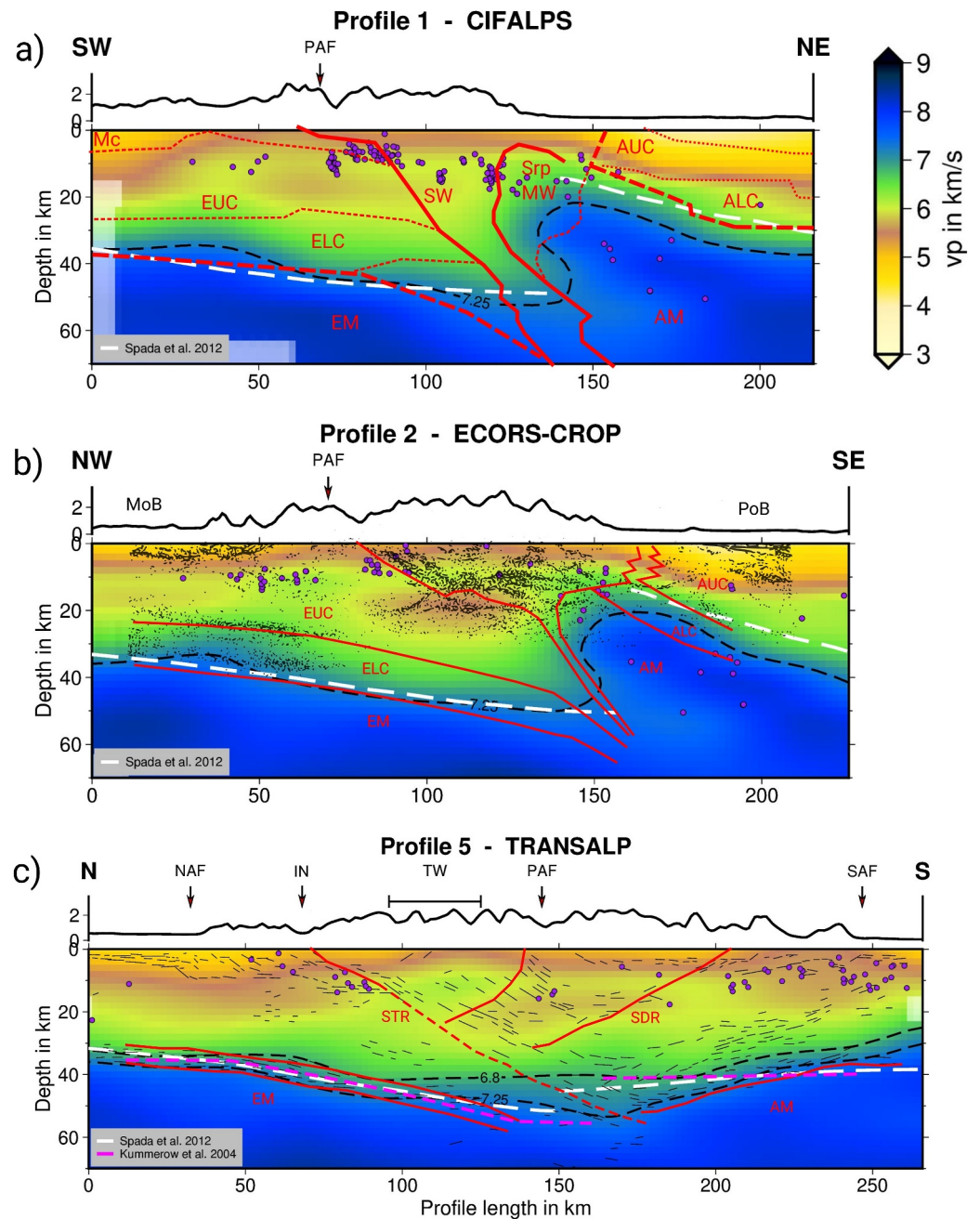
Figure 6. Cross sections through our v_p model along the *CIFALPS*, *ECORS-CROP*, and *TRANSALP* profiles (see map in Figure 5) superimposed with crustal tectonic units (red lines) after Malusà et al. (2021) in (a) and Schmid et al. (2017) in (b). Seismic reflectors (black drawings) in (b) are based on Thouvenot et al. (1996). Seismic reflectors (black) and tectonic boundaries (red) in (c) are based on Gebrande et al. (2006). Events within 30 km of the profiles are marked by purple dots. Moho depths from Spada et al. (2012) (white), Kummerow et al. (2004) (magenta) and our Moho proxy of the $v_p = 7.25$ km/s isoline (black) are shown as dashed lines. Mc—Mesozoic cover; EUC—European upper crust; ELC—European lower crust; EM—European mantle; AUC—Adriatic upper crust; ALC—Adriatic lower crust; AM—Adriatic mantle; SW—subduction wedge; Srp MW—Serpentinized mantle wedge; PAF—Periadriatic Fault; MoB—Molasse basin; PoB—Po basin; NAF—Northern Alpine Front; TW—Tauern Window; SAF—Southern Alpine Front; IN—Inntal Fault; STR—Sub-Tauern Ramp; SDR—Sub-Dolomites Ramp.

5. Discussion

### 5.1. CIFALPS, ECORS-CROP, and TRANSALP

Based on seismic data from the CIFALPS experiment (Zhao et al., 2016) the western Alps have recently been studied with a variety of geophysical methods. One of the key findings is seismic evidence of European continental crust subducted into the Adriatic upper mantle along a serpentinized plate interface (Zhao et al., 2015, 2020). In Figure 6a we show our vp model along the CIFALPS transect overlain by line drawings separating crustal units based on Malusà et al. (2021) (their Figure 13a). Their model is in good agreement with our Moho proxy and the presence of lower crustal velocities at depths of up to 55 km beneath the Ivrea body. At the westernmost tip of the Ivrea body the transition from mantle to crustal velocities matches the location of a serpentinized mantle wedge as proposed by Malusà et al. (2021). We find slightly increased vp/vs values of 1.75–1.76 where Zhao et al. (2020) found a body of low vs in the subduction channel at 50–60 km depth (green star in their Figure 2a). Our European Moho is consistent with Spada et al. (2012) and Malusà et al. (2021) while we image a 5–10 km deeper Moho on the Adriatic side.

In Figure 6b we compare our v_p model along the NW-SE striking ECORS-CROP profile in the Western Alps to the Moho from Spada et al. (2012), outlines of crustal units from Schmid et al. (2017) and seismic reflectors from Thouvenot et al. (1996). Deep crustal velocities beneath the arc and the oversteepened positive anomaly attributed to the Ivrea body are in agreement with Schmid et al. (2017). At shallow depths the reflectivity coincides well with the strong velocity gradients at the bottom of the foreland basins at ≈5 km beneath the Molasse basin and ≈10 km beneath the Po basin. Low velocities at 15–25 km depth southeast of the PAF are correlating well with an area of increased reflectivity. Similar to the CIFALPS profile, based on the tectonic model this mid crustal area of low velocities is located in the eastern part of the European upper crust.

Along TRANSALP our Moho proxy matches Kummerow et al. (2004) and Spada et al. (2012) on the European side and is dipping significantly steeper on the Adriatic side where it reaches ≈30 km beneath the northern Po basin, similar to profile 4. Our Moho proxy also matches the seismic reflection elements along the TRANSALP profile (Gebrande et al., 2006), both at the European and Adria side. Beneath the Tauern Window (TW) higher velocities in the middle crust are found intersecting the reduced velocity anomaly spanning across the whole orogen (Figure 5, Profile 7). We do not find a clear indication of a lower crustal bulge as proposed by Jozi Najafabadi et al. (2022) located to the South of the PAF, but image a horizontal 6.8 km/s v_p-isoline as an upper boundary for the lower crust beneath the Central Alps. Out of the several geological models that have been proposed previously our velocity structure shows the best agreement with the "Lateral Extrusion" scenario (e.g., Gebrande et al., 2006; Jozi Najafabadi et al., 2022, and references therein). Following the interpretation of the "Lateral Extrusion Model" by Jozi Najafabadi et al. (2022) the PAF follows the contrast between upper and lower crustal velocity. In the upper 10 km the Sub-Tauern Ramp is also imaged by seismicity and a slight velocity contrast but the correlation is diminishing at larger depth. Additionally, the Sub-Dolomites Ramp also coincides with a velocity contrast of lower velocities to the West down to approximately 25 km depth. However, the southward dip of the reflector elements beneath the TW can not be reconciled with our new velocity model and a reevaluation of the reflection line might be necessary to settle this long standing debate.

5.2. Mid-Crustal Low Velocities in Western and Central Alps

Consistently decreased velocities in the mid-crust are clearly visible in the depth sections (Figures 4b and 4f; anomalies G and H) and in all cross sections (Figure 5). This feature is narrower in the western arc with ≈50 km width (Figure 4, anomaly G), broadens to more than 100 km in the Central Alps (Figure 4, anomaly H) and is not coherently present in the Eastern Alps. Our reconstruction tests (Figure 3a) show the resolvability of such features for v_p at mid crustal depths. Diehl et al. (2009) likewise observe a prominent low velocity zone at 30 km depth (their Figure 9) beneath the Western and Central Alps which they attribute to the Alpine crustal root. Due to the increased number of arrival times, we are able to parametrize the model with an additional crustal layer compared to Diehl et al. (2009). With this refined vertical resolution we demonstrate that this Alpine Mid Crustal Low Velocity (AMCLV) is mostly separated from the surface by a band of $v_p > 6.0$ km/s (Figure 5). Bagagli et al. (2025) do not image this feature consistently, but likewise observe a decrease in v_p at 20–30 km depth west of the Giudicarie line in the Eastern Central Alps (their Figure 8b) similar to our anomaly H in Figure 4. Menichelli et al. (2023) similarly image an area of low velocity in the Western and Central Alps at mid and lower
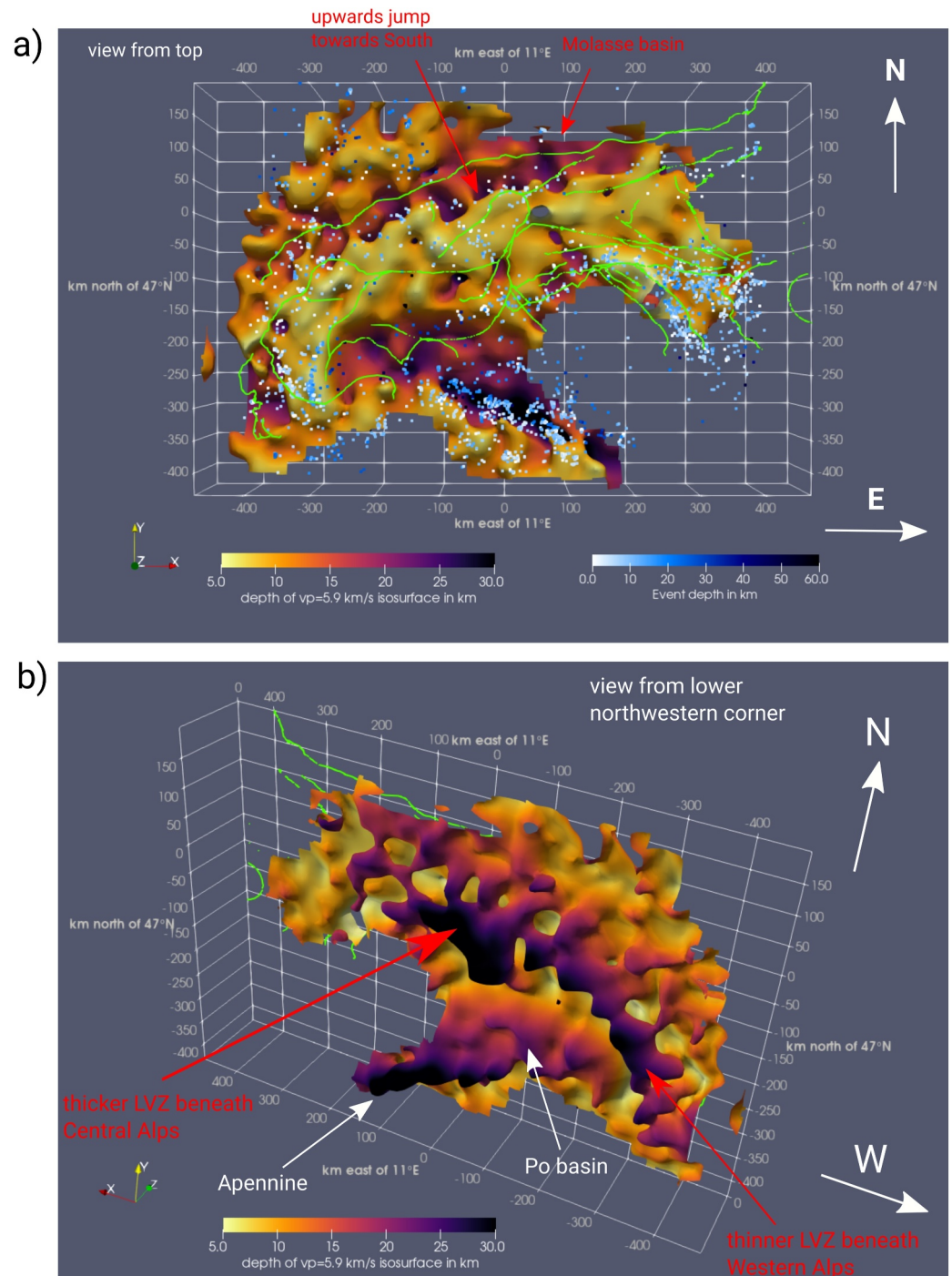
Figure 7. Visualization of the $v_p = 5.9$ km/s iso-velocity surface as an approximation for the transition from upper to middle crust using *ParaView* (Ahrens et al., 2005) with viewing angles from the top (a) and the lower northwestern corner of the model space (b). Fault lines (green) are based on Schmid et al. (2004).

crustal depths. Kästle et al. (2024) also find a prominent decrease of velocity in their v_s model of the Eastern Alps. The smaller scale LET of the Eastern and Eastern Southern Alps from Jozi Najafabadi et al. (2022) images low velocities at 15–20 km beneath a shallower high velocity area along the Tauern Window (TW) (their Figure 9e) which is in agreement with our Profile 7 (Figure 5). Here, in our model the AMCLV is slightly shallower beneath the eastern TW and terminates between 13.5 and 14.0°E.

Figure 7 visualizes this AMCLV in 3D by plotting the v_p = 5.9 km/s iso-velocity surface approximating the transition from upper to mid crustal velocities based on the *GAR1D_McMC* model (Figure S7b in Supporting Information S1). The top-view in Figure 7a reveals a southward dipping surface beneath the Molasse basin in the northern foreland and an upward jump of the iso-surface to ≈5 km South of the Northern Alpine Front which coincides with a band of WSW-ENE oriented shallow seismicity. Figure 7b is looking at the same iso-velocity surface from the lower northwestern corner of the model space. It illustrates the thinner AMCLV along the western arc and its thickening beneath the Central Alps. The AMCLV is partly connected to shallow low velocities on the European side in the Northwest and North and disconnected to the South and Southeast. Thus, we attribute this AMCLV to former European upper crust which has been emplaced at 15–25 km depth due to thrusting during continental collision which resulted in crustal stacking. While the thinner low velocity belt in the Western Alps is in agreement with smaller amounts of collisional shortening (Malusà et al., 2015), Miocene counterclockwise rotation of the Adriatic plate (M. Handy et al., 2010) likely expedited stacking West of the Giudicarie line in the Central Alps. Furthermore, this interpretation matches tectonic outlines along the CIFALPS and ECORS-CROP profiles (Figures 6a and 6b) which assign this AMCLV to the European upper crustal domain. The AMCLV terminates abruptly at the Giudicarie line in the Eastern Central Alps as illustrated by the 1D v_p profiles in Figure 8. Further to the East it is strongly reduced and slightly shallower (Figures 5h and 7b) indicating only minor crustal stacking. The regions of major crustal stacking in the Western and Central arc are showing the deepest crustal root based on our Moho proxy velocity (Figure 9) which is in agreement with previous studies (Kästle et al., 2018; Spada et al., 2012).

5.3. Moho and Dolomites Indenter

As stated above, we define our Moho proxy as the depth of the v_p = 7.25 km/s iso-velocity surface as displayed in Figure 9. First order features such as the shallow Moho of 15–20 km depth beneath the Ivrea zone and a deep crustal root of up to 60 km depth in the Western and Central Alps and in the Northern Apennines are in good agreement with previous studies of the region (Kästle et al., 2024; Lu et al., 2020; Spada et al., 2012). It should be noted that most of the mantle directly beneath the Moho shows a slightly elevated *vp/vs* ratio which might indicate widespread hydration of the mantle due to the complex collision scenario in the area as already has been postulated in the Western Alps by Zhao et al. (2015). Along the northern margin of the Adriatic plate we image Moho depths of 30–35 km which is 5–10 km shallower compared to results from Spada et al. (2012). Beneath the Lepontine Dome in the Western Central Alps between 8.5 and 9.5°E the maximum Moho depths is slightly shallower with ≈45 km. This feature is similarly present in Lu et al. (2020) while only slightly indicated in Spada et al. (2012).

Another anomaly within the generally deepened Moho proxy beneath the arc is visible East of the Giudicarie line where we image Moho depths of 35–40 km at the location of the Dolomites indenter (Pomella et al., 2012; Ratschbacher et al., 1991). In the same area we observe a prominent high velocity zone between 20 and 40 km depth (Figure 4, anomaly J) with a strong negative lateral velocity contrast to the West due to the previously discussed emplacement of upper crust. This contrast is following the Giudicarie line very closely and is strongest between 15 and 40 km depth as the 1D velocity profiles in Figure 8 illustrate. Our reconstruction tests (Figure 3a) verify that a feature of the given amplitude and shape is clearly resolved in the v_p model.

Albeit in less detail, this increased velocity of the Dolomites indenter and an elevated Moho have been imaged by previous works. We note that receiver function and controlled source seismic studies (Michailos et al., 2023; Mroczek & Tilmann, 2021; Spada et al., 2012) which are sensitive to sharp velocity contrasts along interfaces do not image an elevated Moho at the location of the Dolomites indenter. Methods such as LET, ambient noise tomography and wave equation tomography which rely on proxy velocities to infer Moho depths mostly show a shallower Moho and increased velocity east of the Giudicarie line. These features have been attributed to remnants of Permian magmatism (Schuster & Stüwe, 2008) by several studies (Jozi Najafabadi et al., 2022; Lu et al., 2020; Sadeghi-Bagherabadi et al., 2021). Alternatively, Kästle et al. (2024) speculated about underthrust crustal slivers that are being dragged by laterally discontinuous segments of the sinking Alpine slab or crustal deformation resulting from the collision with Adria.

The gradient of the 1D v_p profiles through the southern Dolomites indenter is very similar to the northern Adriatic plate (Figure 8). Thus, we interpret the southern part of the indenter to be a largely undeformed continuation of the northern Adriatic plate. Lower velocities of the southern Dolomites indenter likely are a consequence of downward bending of the Adriatic plate toward the North which also explains its slightly deeper Moho at 35–40 km
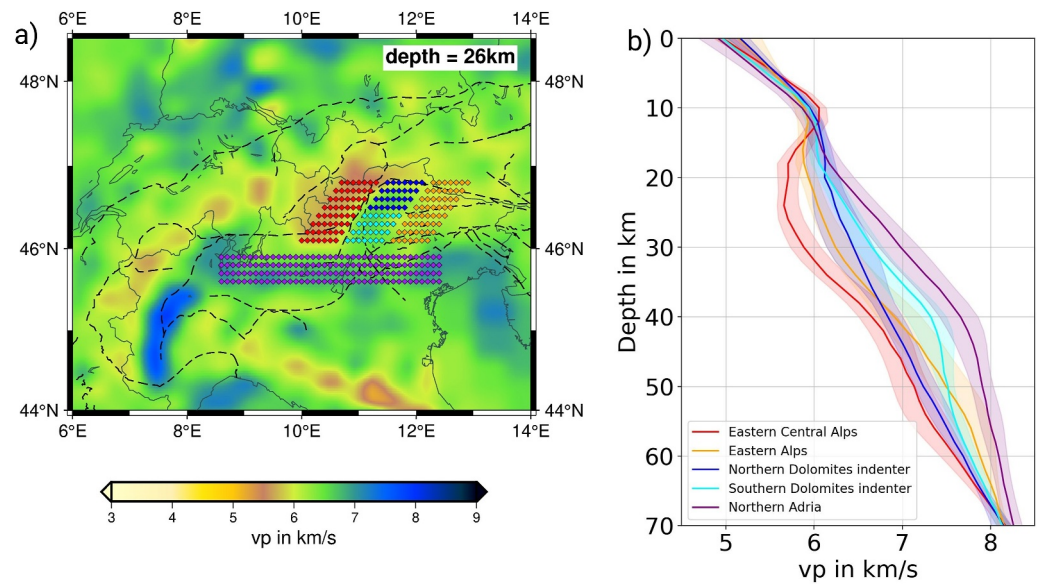
Figure 8. (a) Location of 1D v_p profiles for several regions in the Central and Eastern Alps indicated by colored diamonds plotted on top of the v_p model at 26 km. (b) 1D v_p distribution over depth for the regions in (a). Solid lines and shaded areas mark the average and standard deviation of v_p over depth.
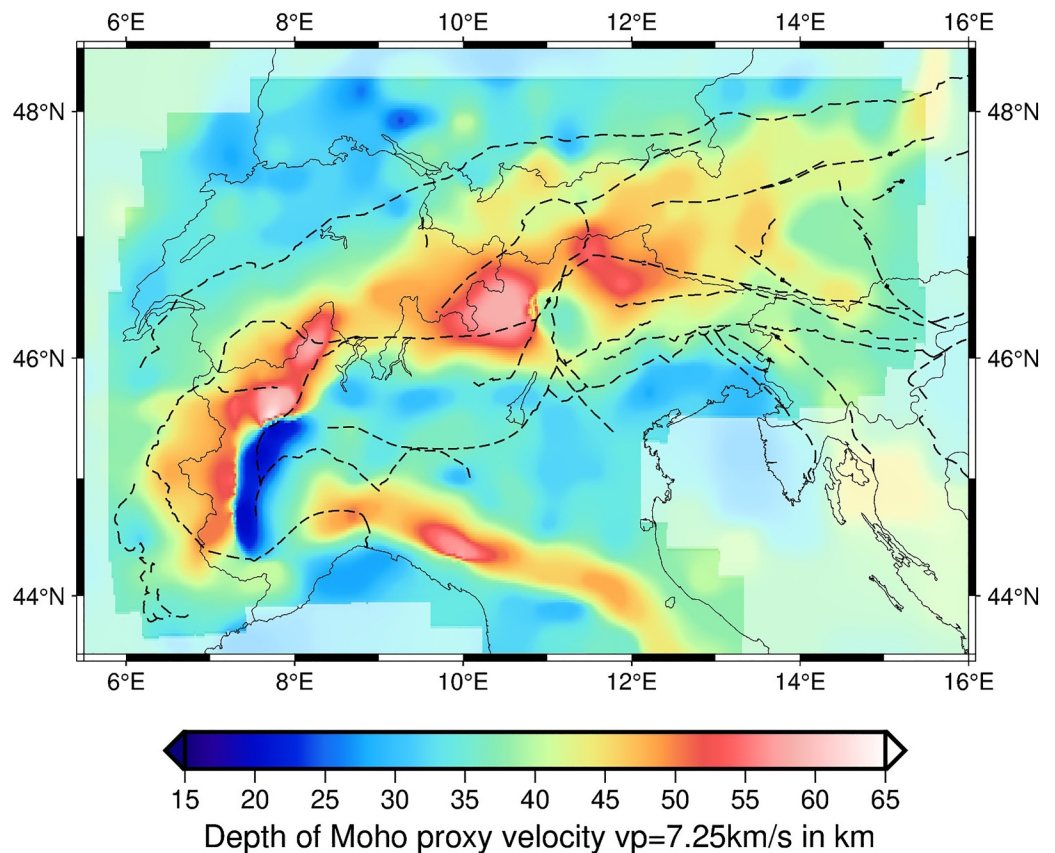
Figure 9. Similar to other LET studies of the area we chose the depth of the $v_p = 7.25$ km/s iso-surface as a Moho proxy. Poorly resolved areas are blurred based on the model resolution at the average Moho depth of ~40 km. Fault lines are based on Schmid et al. (2004).

compared to the "original" Adriatic continental Moho at ≈30 km. Similar to other studies, we image an apparent Moho elevation compared to the region west of the Giudicarie line with a Moho jump of 15–20 km. In comparison to the southern part of the Dolomites indenter, its northern part shows a rather continuous velocity gradient with depth (Figure 8) with strongly decreased velocities in the lower crust and a deeper Moho (Figure 9). We interpret this as thickening of the lower crust and deformation as a result of continental collision and potential remains of Permian magmatism. There is not coherent signature of the Dolomites indenter in the *vp/vs* model (Figure 4).

In the Eastern Alps we observe a consistent shallowing of the Moho toward the East which is in accordance with previous studies as the comparison of our Moho proxy with Spada et al. (2012) in Figure 5h shows. Combined with the less pronounced mid crustal low velocity anomalies (Figures 4b, 4f, and 8) we infer that only minor stacking of European and Adriatic crust took place in the Eastern Alps. Instead, crustal material extruded eastward toward the Pannonian basin (Frisch et al., 1998; Ratschbacher et al., 1991).

6. Conclusion

We present the first orogen-wide 3D *P*- and *S*-wave tomographic velocity model for crust and upper mantle beneath the Greater Alpine region based on local earthquake data collected during the AlpArray project. We use the deep neural network *PhaseNet* to determine 173,841 *P*- and 68,967 *S*-phase arrivals from 2,553 events of $M_L \geq 1.5$ and quantify the horizontal and vertical hypocenter uncertainty as $\sigma_{hor} \approx 0.5$ km and $\sigma_{ver} \approx 3.5$ km, respectively. Based on synthetic reconstruction tests we demonstrate excellent resolution (both, spatially and in amplitude) in the entire crust throughout the orogen, which previously could not be achieved by the numerous local studies in the Alps. We find a belt of consistently decreased velocities in the Western and Central Alps at intermediate crustal levels between 15 and 25 km depth which we have called the Alpine Mid Crustal Low Velocity (AMCLV) anomaly. The AMCLV is terminated sharply by the Dolomites indenter along the Giudicarie line and is less pronounced in the Eastern Alps. Based on its partial connection to the upper crust of the European foreland in the Western and Central Alps we interpret the AMCLV as the former European upper crust that has been accumulated stacked during collision. Along the Central and Eastern Alps the shallow seismicity indicating the active deformation is aligned with the connection of the AMCLV to the European foreland. The AMCLV is most prominent directly West of the Giudicarie line where Miocene counterclockwise rotation of the Adriatic plate further facilitated crustal stacking as a consequence of shortening. Furthermore, this matches the observed deep crustal root beneath the Western and Central Alps with Moho depths of up to 60 km. In the Eastern Alps, the AMCLV is less coherent and smaller in amplitude indicating, if any, only minor amounts of crustal stacking. East of the Giudicarie line we image the Dolomites indenter, which is offsetting the Moho by 20–25 km. We see a clear difference in the seismic signature of the Dolomites indenter between its northern and southern part. We interpret its southern part to be a largely undeformed continuation of the northwards dipping northern Adriatic plate based on their similar 1D velocity profiles. The northern part shows a strongly thickened lower crust most likely due to deformation during indentation with additional potential remnants of Permian magmatism. Reflection seismic images and tectonic interpretations from previous studies of the CIFALPS, ECORS-CROP and TRANSALP transects are generally matching well with our new velocity model. Along the TRANSALP profile we image an anomaly of slightly northward dipping increased velocities beneath the Tauern window which does not conform with structures imaged by seismic reflection data from previous works and more detailed reanalysis of the reflection seismic profiles with modern techniques might be necessary to solve this contradiction.

Conflict of Interest

The authors declare no conflicts of interest relevant to this study.

Data Availability Statement

The final velocity model is published at RADAR4KIT (Rietbrock & Braszus, 2025). A catalog of the relocated seismicity and all used arrival time picks is published there as well. All seismic waveform data is publicly available and was accessed via the FDSN web service client for ObsPy (Krischer et al., 2015) (last data download 2023 November 9). We used data from the following temporary and permanent seismic networks: BW (Department of Earth and Environmental Sciences, Geophysical Observatory, University of Munchen, 2001), CH (SED at ETH Zurich, 1983), CR (University of Zagreb, 2001), CZ (Charles University in Prague (Czech

et al., 1973), FR (RESIF, 1995), GE (GEOFON Data Centre, 1993), GU (University of Genoa, 1967), HU (Kövesligethy Radó Seismological Observatory (Geodetic And Geophysical Institute, Research Centre For Astronomy And Earth Sciences, Hungarian Academy Of Sciences (MTA CSFK GGI KRSZO)), 1992), IV (Istituto Nazionale di Geofisica e Vulcanologia (INGV), 2005), MN (MedNet Project Partner Institutions, 1988), MT (French Landslide Observatory—Seismological Datacenter/RESIF, 2006), NI (OGS (Istituto Nazionale di Oceanografia e di Geofisica Sperimentale) and University of Trieste, 2002), OE (ZAMG—Zentralanstalt für Meterologie und Geodynamik, 1987), OX (Istituto Nazionale di Oceanografia e di Geofisica Sperimentale— OGS, 2016), PL, RD (RESIF, 2018), RF (University of Trieste, 1993), SI, SK (ESI SAS; Former GPI SAS (Geophysical Institute Of The Slovak Academy Of Sciences), 2004), SL (Slovenian Environment Agency, 1990), ST (Geological Survey-Provincia Autonoma di Trento, 1981), XT (Zhao et al., 2018), YI (Chaljub, 2017), YW (Guéguen et al., 2017), Z3 (AlpArray Seismic Network, 2015), ZS (Heit et al., 2017), 1N (Malet et al., 2015), 1P (Ritter et al., 2014), 3C (Ohrnberger et al., 2023), 4H, 8C (Helmstetter et al., 2020), 8D (Swiss Seismological Service (SED) At ETH Zurich, 2005).

References

Ahrens, J., Geveci, B., & Law, C. (2005). In C. D. Hansen & C. R. Johnson (Eds.), *Visualization handbook* (pp. 717–731). Elsevier Inc. Retrieved from https://www.sciencedirect.com/book/9780123875822/visualization-handbook

AlpArray Seismic Network. (2015). *AlpArray Seismic Network (AASN) temporary component*. AlpArray Working Group. https://doi.org/10.12686/ALPARRAY/Z3_2015

Arcoraci, L., Miconi, L., Cheloni, D., Colini, L., Di Maro, R., Lisi, A., et al. (2020). *Bollettino Sismico Italiano (BSI), I quadrimestre 2020*. Istituto Nazionale di Geofisica e Vulcanologia (INGV). https://doi.org/10.13127/BSI/202001

Bagagli, M., Molinari, I., Diehl, T., & Kissling, E. (2025). Local earthquake tomography of the Alpine region from 24 years of data. *Geophysical Journal International*, *241*(1), 454–473. https://doi.org/10.1093/gji/ggaf028

Bagagli, M., Molinari, I., Diehl, T., Kissling, E., Giardini, D., & AlpArray Working Group. (2022). The AlpArray research seismicity-catalogue. *Geophysical Journal International*, *231*(2), 921–943. https://doi.org/10.1093/gji/ggac226

Bayer, R., Carozzo, M., Lanza, R., Miletto, M., & Rey, D. (1989). Gravity modelling along the ECORS-CROP vertical seismic reflection profile through the Western Alps. *Tectonophysics*, *162*(3), 203–218. https://doi.org/10.1016/0040-1951(89)90244-8

Bigi, G., Castellarin, A., Coli, M., Dal Piaz, G., Sartori, R., Scandone, P., & Vai, G. (1990). *Structural model of Italy, 1:500.000* (Vol. 114, pp. 81–110). Quaderni de La Ricerca Scientifica, C.N.R.

Bleibinhaus, F., & Gebrande, H. (2006). Crustal structure of the Eastern Alps along the TRANSALP profile from wide-angle seismic tomography. *Tectonophysics*, *414*(1), 51–69. https://doi.org/10.1016/j.tecto.2005.10.028

Bousquet, R., Schmid, S., Zeilinger, G., Oberhänsli, R., Rosenberg, C., Molli, G., et al. (2012). *Tectonic framework of the alps*. CCGM/CGMW (Commission for the Geological Map of the World, Paris).

Braszus, B., Rietbrock, A., Haberland, C., & Ryberg, T. (2024). AI based 1-D P- and S-wave velocity models for the greater alpine region from local earthquake data. *Geophysical Journal International*, *237*(2), 916–930. https://doi.org/10.1093/gji/ggae077

Brückl, E. (2011). Lithospheric structure and tectonics of the Eastern Alps—Evidence from new seismic data. In D. Closson (Ed.), *Tectonics (chap. 2)*. IntechOpen. Rijeka. https://doi.org/10.5772/14364

Brückl, E., Bodoky, T., Hegedus, E., Hrubcova, P., Gosar, A., Grad, M., et al. (2003). ALP 2002 seismic experiment. *Studia Geophysica et Geodaetica*, *47*(3), 671–679. https://doi.org/10.1023/A:1024780022139

Carminati, E., Lustrino, M., & Doglioni, C. (2012). Geodynamic evolution of the central and western Mediterranean: Tectonics vs. igneous petrology constraints. *Tectonophysics*, *579*, 173–192. https://doi.org/10.1016/j.tecto.2012.01.026

Chaljub, E. (2017). Saint-Guérin Arch Dam Experiment, 2015-2016, code YI, funded by chaire Pereniti (Grenoble INP, EDF), Université Grenoble Alpes, instrumented by RESIF-SISMOB [Dataset]. *RESIF - Réseau Sismologique et géodésique Français*. https://doi.org/10.15778/RESIF.YI2015

Charles University in Prague (Czech), Institute of Geonics, Institute of Geophysics, Academy of Sciences of the Czech Republic, Institute of Physics of the Earth Masaryk University (Czech), and Institute of Rock Structure and Mechanics. (1973). Czech regional seismic network [Dataset]. *International Federation of Digital Seismograph Networks*. https://doi.org/10.7914/SN/CZ

Department of Earth and Environmental Sciences, Geophysical Observatory, University of Munchen. (2001). BayernNetz [Dataset]. *International Federation of Digital Seismograph Networks*. https://doi.org/10.7914/SN/BW

Dewey, J., Helman, M., Knott, S., Turco, E., & Hutton, D. (1989). Kinematics of the western Mediterranean. *Geological Society, London, Special Publications*, *45*(1), 265–283. https://doi.org/10.1144/GSL.SP.1989.045.01.15

Diehl, T., Husen, S., Kissling, E., & Deichmann, N. (2009). High-resolution 3-D P-wave model of the Alpine crust. *Geophysical Journal International*, *179*(2), 1133–1147. https://doi.org/10.1111/j.1365-246X.2009.04331.x

Diehl, T., Kissling, E., Herwegh, M., & Schmid, S. (2021). Improving absolute hypocenter accuracy with 3D Pg and Sg body-wave inversion procedures and application to earthquakes in the Central Alps Region. *Journal of Geophysical Research: Solid Earth*, *126*(12), e2021JB022155. https://doi.org/10.1029/2021JB022155

Eberhart-Phillips, D. (1990). Three-dimensional P and S velocity structure in the Coalinga Region, California. *Journal of Geophysical Research*, *95*(B10), 15343–15363. https://doi.org/10.1029/JB095iB10p15343

Eberhart-Phillips, D., Thurber, C., Rietbrock, A., Fry, B., Reyners, M., & Lanza, F. (2024). Simul2023: A flexible program for inversion of earthquake data for 3-D velocity and hypocenters or 3-D Q [Software]. *Zenodo*. https://doi.org/10.5281/zenodo.10695070

ECORS-CROP DSS Group. (1989). A new picture of the Moho under the Western Alps. *Nature*, *337*(6204), 249–251. https://doi.org/10.1038/337249a0

ESI SAS; Former GPI SAS (Geophysical Institute Of The Slovak Academy Of Sciences). (2004). National Network of Seismic Stations of Slovakia [Dataset]. *GFZ Data Services*. https://doi.org/10.14470/FX099882

French Landslide Observatory—Seismological Datacenter / RESIF. (2006). Observatoire Multi-disciplinaire des Instabilités de Versants (OMIV) [Dataset]. *RESIF—Réseau Sismologique et géodésique Français*. https://doi.org/10.15778/RESIF.MT

Frisch, W., Kuhlemann, J., Dunkl, I., & Brügel, A. (1998). Palinspastic reconstruction and topographic evolution of the Eastern Alps during late Tertiary tectonic extrusion. *Tectonophysics*, *297*(1), 1–15. https://doi.org/10.1016/S0040-1951(98)00160-7

Froitzheim, N., Schmid, S., & Frey, M. (1996). Mesozoic paleogeography and the timing of eclogitefacies metamorphism in the Alps: A working hypothesis. *Eclogae Geologicae Helvetiae*, *891*(1), 81–110. https://doi.org/10.5169/seals-167895

Fukao, Y., Obayashi, M., Inoue, H., & Nenbai, M. (1992). Subducting slabs stagnant in the mantle transition zone. *Journal of Geophysical Research*, *97*(B4), 4809–4822. https://doi.org/10.1029/91JB02749

Gebrande, H., Lüschen, E., Bopp, M., Bleibinhaus, F., Lammerer, B., Oncken, O., & Marcello, B. (2006). Publisher's correction to "first deep seismic reflection images of the eastern alps reveal giant crustal wedges and transcrustal ramps". *Geophysical Research Letters*, *33*(15). https://doi.org/10.1029/2006GL026618

GEOFON Data Centre. (1993). GEOFON Seismic Network [Dataset]. *Deutsches GeoForschungsZentrum GFZ*. https://doi.org/10.14470/TR560404

Geological Survey-Provincia Autonoma di Trento. (1981). Trentino Seismic Network [Dataset]. *International Federation of Digital Seismograph Networks*. https://doi.org/10.7914/SN/ST

Guéguen, P., Coutant, O., Langlais, M., & RESIF. (2017). Maurienne Seismic Swarm 2017–2018 [Dataset]. *RESIF—Réseau Sismologique et géodésique Français*. https://doi.org/10.15778/RESIF.YW2017

Hammerl, C., & Brückl, E. (2014). Eduard Suess' conception of the Alpine orogeny related to geophysical data and models. *Austrian Journal of Earth Sciences*, *107*, 94–114.

Handy, M., Schmid, S., Bousquet, R., Kissling, E., & Bernoulli, D. (2010). Recoiling plate-tectonic reconstructions of Alpine Tethys with the geological-geophysical record of spreading and subduction in the Alps. *Earth-Science Reviews*, *102*, 121–158. https://doi.org/10.1016/j.earscirev.2010.06.002

Handy, M., Ustaszewski, K., & Kissling, E. (2014). Reconstructing the Alps–Carpathians–Dinarides as a key to understanding switches in subduction polarity, slab gaps and surface motion. *International Journal of Earth Sciences*, *104*, 1–26. https://doi.org/10.1007/s00531-014-1060-3

Handy, M. R., Giese, J., Schmid, S. M., Pleuger, J., Spakman, W., Onuzi, K., & Ustaszewski, K. (2019). Coupled crust-mantle response to slab tearing, bending, and rollback along the Dinaride-Hellenide Orogen. *Tectonics*, *38*(8), 2803–2828. https://doi.org/10.1029/2019TC005524

Haslinger, F., Kissling, E., Ansorge, J., Hatzfeld, D., Papadimitriou, E., Karakostas, V., et al. (1999). 3D crustal structure from local earthquake tomography around the Gulf of Arta (Ionian region, NW Greece). *ELSEVIER Tectonophysics*, *304*(3), 201–218. https://doi.org/10.1016/S0040-1951(98)00298-4

Heit, B., Cristiano, L., Haberland, C., Tilmann, F., Pesaresi, D., Jia, Y., et al. (2021). The SWATH-D seismological network in the Eastern Alps. *Seismological Research Letters*, *92*(3), 1592–1609. https://doi.org/10.1785/0220200377

Heit, B., Weber, M., Tilmann, F., Haberland, C., Jia, Y., Carraro, C., et al. (2017). The Swath-D Seismic Network in Italy and Austria [Dataset]. *GFZ Data Services*. https://doi.org/10.14470/MF7562601148

Helmstetter, A., & Guéguen, P., & RESIF. (2020). Seismic network 8C: Monitoring swarms in the Mont-Blanc and Vallorcine area (RESIF—SISMOB) [Dataset]. *RESIF—Réseau Sismologique et géodésique Français*. https://doi.org/10.15778/RESIF.8C2019

Hetényi, G., Molinari, I., Clinton, J., Bokelmann, G., Bondár, I., Crawford, W., et al. (2018). The AlpArray seismic network: A large-scale European experiment to image the Alpine Orogen. *Surveys in Geophysics*, *39*(5), 1009–1033. https://doi.org/10.1007/s10712-018-9472-4

Hetényi, G., Plomerová, J., Bianchi, I., Kampfová Exnerová, H., Bokelmann, G., Handy, M. R., & Babuška, V. (2018). From mountain summits to roots: Crustal structure of the Eastern Alps and Bohemian Massif along longitude 13.3°E. *Tectonophysics*, *744*(2), 239–255. https://doi.org/10.1016/j.tecto.2018.07.001

Husen, S., Kissling, E., Flueh, E., & Asch, G. (1999). Accurate hypocentre determination in the seismogenic zone of the subducting Nazca Plate in northern Chile using a combined on-/offshore network. *Geophysical Journal International*, *138*(3), 687–701. https://doi.org/10.1046/j.1365-246x.1999.00893.x

Istituto Nazionale di Geofisica e Vulcanologia (INGV). (2005). Rete sismica nazionale (rsn) [Dataset]. *Istituto Nazionale di Geofisica e Vulcanologia (INGV)*. https://doi.org/10.13127/SD/X0FXNH7QFY

Istituto Nazionale di Oceanografia e di Geofisica Sperimentale—OGS. (2016). North-East Italy Seismic Network [Dataset]. *FDSN*. https://doi.org/10.7914/SN/OX

Jozi Najafabadi, A., Haberland, C., Le Breton, E., Handy, M., Verwater, V., Heit, B., & Weber, M. (2022). Constraints on crustal structure in the vicinity of the Adriatic indenter (European Alps) from Vp and Vp/Vs local earthquake tomography. *Journal of Geophysical Research: Solid Earth*, *127*(2), e2021JB023160. https://doi.org/10.1029/2021JB023160

Kästle, E., El-Sharkawy, A., Boschi, L., Meier, T., Rosenberg, C., Bellahsen, N., et al. (2018). Surface wave tomography of the Alps using ambient-noise and earthquake phase velocity measurements. *Journal of Geophysical Research: Solid Earth*, *123*(2), 1770–1792. https://doi.org/10.1002/2017JB014698

Kästle, E., Tilmann, F., & AlpArray and Swath-D Working Groups. (2024). Anisotropic reversible-jump McMC shear-velocity tomography of the Eastern Alpine Crust. *Geochemistry, Geophysics, Geosystems*, *25*(3), e2023GC011238. https://doi.org/10.1029/2023GC011238

Kissling, E., Schmid, S. M., Lippitsch, R., Ansorge, J., & Fügenschuh, B. (2006). Lithosphere structure and tectonic evolution of the Alpine arc: New evidence from high-resolution teleseismic tomography. *Geological Society, London, Memoirs*, *32*(1), 129–145. https://doi.org/10.1144/GSL.MEM.2006.032.01.08

Kövesligethy Radó Seismological Observatory (Geodetic And Geophysical Institute, Research Centre For Astronomy And Earth Sciences, Hungarian Academy Of Sciences (MTA CSFK GGI KRSZO)). (1992). Hungarian National Seismological Network [Dataset]. *GFZ Data Services*. https://doi.org/10.14470/UH028726

Krischer, L., Megies, T., Barsch, R., Beyreuther, M., Lecocq, T., Caudron, C., & Wassermann, J. (2015). ObsPy: A bridge for seismology into the scientific Python ecosystem. *Computational Science & Discovery*, *8*(1), 014003. https://doi.org/10.1088/1749-4699/8/1/014003

Kummerow, J., Kind, R., Oncken, O., Giese, P., Ryberg, T., Wylegalla, K., & Scherbaum, F. (2004). A natural and controlled source seismic profile through the Eastern Alps: TRANSALP. *Earth and Planetary Science Letters*, *225*(1), 115–129. https://doi.org/10.1016/j.epsl.2004.05.040

Levato, L., Pruniaux, B., Burri, M., Escher, A., Olivier, R., Sellami, S., & Wagner, J.-J. (1993). Processing and preliminary results of NFP/PNR20 seismic reflection profiles from the Western Swiss Alps. *Tectonophysics*, *219*(1), 93–107. https://doi.org/10.1016/0040-1951(93)90289-V

Lippitsch, R., Kissling, E., & Ansorge, J. (2003). Upper mantle structure beneath the Alpine orogen from high-resolution teleseismic tomography. *Journal of Geophysical Research*, *108*(B8), 2376. https://doi.org/10.1029/2002JB002016

Lu, Y., Stehly, L., Brossier, R., & Paul, A. (2020). Imaging Alpine crust using ambient noise wave-equation tomography. *Geophysical Journal International*, *222*(1), 69–85. https://doi.org/10.1093/gji/ggaa145

Lüschen, E., Lammerer, B., Gebrande, H., Millahn, K., & Nicolich, R. (2004). Orogenic structure of the Eastern Alps, Europe, from TRANSALP deep seismic reflection profiling. *Tectonophysics*, *388*(1–4), 85–102. https://doi.org/10.1016/j.tecto.2004.07.024

Malet, J.-P., Hibert, C., Radiguet, M., Gautier, S., Larose, E., Amitrano, D., et al. (2015). French Landslide Observatory—OMIV (Temporary data) (MT-campagne) (RESIF—SISMOB) [Dataset]. *RESIF—Réseau Sismologique et géodésique Français*. https://doi.org/10.15778/RESIF.1N2015

Malusà, M. G., Faccenna, C., Baldwin, S. L., Fitzgerald, P. G., Rossetti, F., Balestrieri, M. L., et al. (2015). Contrasting styles of (U)HP rock exhumation along the Cenozoic Adria-Europe plate boundary (Western Alps, Calabria, Corsica). *Geochemistry, Geophysics, Geosystems*, *16*(6), 1786–1824. https://doi.org/10.1002/2015GC005767

Malusà, M. G., Guillot, S., Zhao, L., Paul, A., Solarino, S., Dumont, T., et al. (2021). The deep structure of the Alps based on the CIFALPS seismic experiment: A synthesis. *Geochemistry, Geophysics, Geosystems*, *22*(3), e2020GC009466. https://doi.org/10.1029/2020GC009466

MedNet Project Partner Institutions. (1988). Mediterranean Very Broadband Seismographic Network (MedNet) [Dataset]. *Istituto Nazionale di Geofisica e Vulcanologia (INGV)*. https://doi.org/10.13127/SD/FBBBTDTD6Q

Menichelli, I., De Gori, P., Lucente, F. P., Improta, L., & Chiarabba, C. (2023). Lithosphere structure, processes, and physical state of the alpine-Apennine system. *Journal of Geophysical Research: Solid Earth*, *128*(4), e2023JB026411. https://doi.org/10.1029/2023JB026411

Michailos, K., Hetényi, G., Scarponi, M., Stipčević, J., Bianchi, I., Bonatto, L., et al. (2023). Moho depths beneath the European Alps: A homogeneously processed map and receiver functions database. *Earth System Science Data*, *15*(5), 2117–2138. https://doi.org/10.5194/essd-15-2117-2023

Mousavi, S., Ellsworth, W., Weiqiang, Z., Chuang, L., & Beroza, G. (2020). Earthquake transformer—An attentive deep-learning model for simultaneous earthquake detection and phase picking. *Nature Communications*, *11*(1), 3952. https://doi.org/10.1038/s41467-020-17591-w

Mroczek, S., & Tilmann, F. (2021). Joint ambient noise auto-correlation and receiver function analysis of the Moho. *Geophysical Journal International*, *225*(3), 1920–1934. https://doi.org/10.1093/gji/ggab065

OGS (Istituto Nazionale di Oceanografia e di Geofisica Sperimentale) and University of Trieste. (2002). North-East Italy Broadband Network [Dataset]. *International Federation of Digital Seismograph Networks*. https://doi.org/10.7914/SN/NI

Ohrnberger, M., Dahm, T., Krüger, F., Hannemann, K., & Korn, M. (2023). University of Potsdam Experimental 3D-3C Array [Dataset]. *GFZ Data Services*. https://doi.org/10.14470/1N671943

Pomella, H., Stipp, M., & Fügenschuh, B. (2012). Thermochronological record of thrusting and strike-slip faulting along the Giudicarie fault system (Alps, Northern Italy). *Tectonophysics*, *579*, 118–130. https://doi.org/10.1016/j.tecto.2012.04.015

Ratschbacher, L., Frisch, W., Hans-Gert, L., & Merle, O. (1991). Lateral extrusion in the eastern Alps, PArt 2: Structural analysis. *Tectonics*, *10*(2), 257–271. https://doi.org/10.1029/90TC02623

Reiter, F., Freudenthaler, C., Hausmann, H., Ortner, H., Lenhardt, W., & Brandner, R. (2018). Active seismotectonic deformation in front of the dolomites indenter, eastern Alps. *Tectonics*, *37*(12), 4625–4654. https://doi.org/10.1029/2017TC004867

RESIF. (1995). RESIF-RLBP French Broad-band network, RESIF-RAP strong motion network and other seismic stations in metropolitan France [Dataset]. *RESIF—Réseau Sismologique et géodésique Français*. https://doi.org/10.15778/RESIF.FR

RESIF. (2018). CEA/DASE broad-band permanent network in metropolitan France [Dataset]. *RESIF—Réseau Sismologique et géodésique Français*. https://doi.org/10.15778/RESIF.RD

Rietbrock, A., & Braszus, B. (2025). Dataset: A comprehensive 3D velocity model for the European Alps based on local earthquake tomography [Dataset]. RADAR4KIT. https://doi.org/10.35097/jn7v3bktz9m5cx3d

Ritter, J. R. R., Schmidt, B., Haberland, C., & Weber, M. (2014). DEEP-TEE Phase 1 [Dataset]. *GFZ Data Services*. https://doi.org/10.14470/6C709520

Ross, Z. E., Meier, M., Hauksson, E., & Heaton, T. H. (2018). Generalized seismic phase detection with deep learning. *Bulletin of the Seismological Society of America*, *108*(5A), 2894–2901. https://doi.org/10.1785/0120180080

Ryberg, T., & Haberland, C. (2019). Bayesian simultaneous inversion for local earthquake hypocentres and 1-D velocity structure using minimum prior knowledge. *Geophysical Journal International*, *218*(2), 840–854. https://doi.org/10.1093/gji/ggz177

Sadeghi-Bagherabadi, A., Vuan, A., Aoudia, A., Parolai, S., & The AlpArray and AlpArray-Swath-D Working Group. (2021). High-resolution crustal S-wave velocity model and Moho Geometry beneath the Southeastern Alps: New insights from the SWATH-D experiment. *Frontiers in Earth Science*, *9*, 641113. https://doi.org/10.3389/feart.2021.641113

Schmid, S., Bernoulli, D., Fügenschuh, B., Matenco, L., Schefer, S., Schuster, R., et al. (2008). The Alpine-Carpathian-Dinaridic orogenic system: Correlation and evolution of tectonic units. *Swiss Journal of Geosciences*, *101*(1), 139–183. https://doi.org/10.1007/s00015-008-1247-3

Schmid, S., Fügenschuh, B., Kissling, E., & Schuster, R. (2004). Tectonic map and overall architecture of the alpine orogen. *Eclogae Geologicae Helvetiae*, *97*(1), 93–117. https://doi.org/10.1007/s00015-004-1113-x

Schmid, S., Kissling, E., Diehl, T., van Hinsbergen, D., & Molli, G. (2017). Ivrea mantle wedge, arc of the Western Alps, and kinematic evolution of the Alps–Apennines orogenic system. *Swiss Journal of Geosciences*, *110*(2), 581–612. https://doi.org/10.1007/s00015-016-0237-0

Schuster, R., & Stüwe, K. (2008). Permian metamorphic event in the Alps. *Geology*, *36*(8), 603–606. https://doi.org/10.1130/G24703A.1

SED at ETH Zurich. (1983). National Seismic Networks of Switzerland [Dataset]. *ETH Zürich*. https://doi.org/10.12686/SED/NETWORKS/CH

Slovenian Environment Agency. (1990). Seismic Network of the Republic of Slovenia [Dataset]. *International Federation of Digital Seismograph Networks*. https://doi.org/10.7914/SN/SL

Solarino, S., Malusà, M. G., Eva, E., Guillot, S., Paul, A., Schwartz, S., et al. (2018). Mantle wedge exhumation beneath the Dora-Maira (U)HP dome unravelled by local earthquake tomography (Western Alps). *Lithos*, *296–299*, 623–636. https://doi.org/10.1016/j.lithos.2017.11.035

Spada, M., Bianchi, I., Kissling, E., Agostinetti, N., & Wiemer, S. (2012). Combining controlled-source seismology and receiver function information to derive 3-D Moho topography for Italy. *Geophysical Journal International*, *194*(2), 1050–1068. https://doi.org/10.1093/gji/ggt148

Swiss Seismological Service (SED) At ETH Zurich. (2005). Temporary deployments in Switzerland associated with aftershocks and other seismic sequences [Dataset]. *ETH Zurich*. https://doi.org/10.12686/SED/NETWORKS/8D

Thouvenot, F., Paul, A., Sénéchal, G., Hirn, A., & Nicolich, R. (1996). Comparison between two techniques of line-drawing migration (ray-tracing and common tangent method). *Bulletin de la Societe Geologique de France*, *170*, 53–59.

Thurber, C. H. (1983). Earthquake locations and three-dimensional crustal structure in the Coyote Lake Area, central California. *Journal of Geophysical Research*, *88*(B10), 8226–8236. https://doi.org/10.1029/JB088iB10p08226

Toomey, D. R., & Foulger, G. R. (1989). Tomographic inversion of local earthquake data from the Hengill-Grensdalur Central Volcano Complex, Iceland. *Journal of Geophysical Research*, *94*(B12), 17497–17510. https://doi.org/10.1029/JB094iB12p17497

Ueida, L., Tian, D., Leong, W. J., Schlitzer, W., Grund, M., Jones, M., et al. (2023). PyGMT: A Python interface for the Generic Mapping Tools [Software]. *Zenodo*. https://doi.org/10.5281/zenodo.7772533

Um, J., & Thurber, C. (1987). A fast algorithm for two-point seismic ray tracing. *Bulletin of the Seismological Society of America*, *77*(3), 972–986. https://doi.org/10.1785/BSSA0770030972

University of Genoa. (1967). Regional Seismic Network of North Western Italy [Dataset]. *International Federation of Digital Seismograph Networks*. https://doi.org/10.7914/SN/GU

University of Trieste. (1993). Friuli Venezia Giulia Accelerometric Network [Dataset]. *International Federation of Digital Seismograph Networks*. https://doi.org/10.7914/SN/RF

University of Zagreb. (2001). Croatian Seismograph Network [Dataset]. *International Federation of Digital Seismograph Networks*. https://doi.org/10.7914/SN/CR

Valasek, P., Mueller, S., Frei, W., & Holliger, K. (1991). Results of NFP 20 seismic reflection profiling along the Alpine section of the European Geotraverse (EGT). *Geophysical Journal International*, *105*(1), 85–102. https://doi.org/10.1111/j.1365-246X.1991.tb03446.x

van der Hilst, R. D., Engdahl, E. R., & Spakman, W. (1993). Tomographic inversion of P and pP data for aspherical mantle structure below the northwest Pacific region. *Geophysical Journal International*, *115*(1), 264–302. https://doi.org/10.1111/j.1365-246X.1993.tb05603.x

Weiqiang, Z., & Beroza, G. (2018). PhaseNet: A deep-neural-network-based seismic arrival time picking method. *Geophysical Journal International*, *216*(1), 261–273. https://doi.org/10.1093/gji/ggy423

Wessel, P., Smith, W. H. F., Scharroo, R., Luis, J., & Wobbe, F. (2013). Generic mapping tools: Improved version released [Software]. *Eos, Transactions American Geophysical Union*, *94*(45), 409–410. https://doi.org/10.1002/2013EO450001

Woollam, J., Münchmeyer, J., Tilmann, F., Rietbrock, A., Lange, D., Bornstein, T., et al. (2022). SeisBench—A toolbox for machine learning in seismology. *Seismological Research Letters*, *93*(3), 1695–1709. https://doi.org/10.1785/0220210324

ZAMG—Zentralanstalt für Meterologie und Geodynamik. (1987). Austrian Seismic Network [Dataset]. *International Federation of Digital Seismograph Networks*. https://doi.org/10.7914/SN/OE

Zhao, L., Malusà, M., Yuan, H., Paul, A., Guillot, S., Lu, Y., et al. (2020). Evidence for a serpentinized plate interface favouring continental subduction. *Nature Communications*, *11*(1), 2171. https://doi.org/10.1038/s41467-020-15904-7

Zhao, L., Paul, A., Guillot, S., Solarino, S., Malusà, M., Zheng, T., et al. (2015). First seismic evidence for continental subduction beneath the Western Alps. *Geology*, *43*(9), 815–818. https://doi.org/10.1130/G36833.1

Zhao, L., Paul, A., Solarino, S., & RESIF. (2016). Seismic network YP: CIFALPS temporary experiment (China-Italy-France Alps seismic transect) [Dataset]. *RESIF—Réseau Sismologique et géodésique Français*. https://doi.org/10.15778/RESIF.YP2012

Zhao, L., Paul, A., Solarino, S., & RESIF. (2018). Seismic network XT: CIFALPS-2 temporary experiment (China-Italy-France Alps seismic transect) [Dataset]. *RESIF—Réseau Sismologique et géodésique Français*. https://doi.org/10.15778/RESIF.XT2018